RAMAN SPECTRA OF THE B MODE OF THE FERROELASTIC COMPOUND $Rb_4LiH_3(SO_4)_4$ AS A FUNCTION OF TEMPERATURE

OKTAY AKTAS

Library and
Archives Canada

Published Heritage
Branch

395 Wellington Street
Ottawa ON K1A 0N4
Canada

Bibliothèque et
Archives Canada

Direction du
Patrimoine de l'édition

395, rue Wellington
Ottawa ON K1A 0N4
Canada

Your file Votre référence
ISBN: 978-0-494-47847-9
Our file Notre référence
ISBN: 978-0-494-47847-9

NOTICE:
The author has granted a non-exclusive license allowing Library and Archives Canada to reproduce, publish, archive, preserve, conserve, communicate to the public by telecommunication or on the Internet, loan, distribute and sell theses worldwide, for commercial or non-commercial purposes, in microform, paper, electronic and/or any other formats.

The author retains copyright ownership and moral rights in this thesis. Neither the thesis nor substantial extracts from it may be printed or otherwise reproduced without the author's permission.

AVIS:
L'auteur a accordé une licence non exclusive permettant à la Bibliothèque et Archives Canada de reproduire, publier, archiver, sauvegarder, conserver, transmettre au public par télécommunication ou par l'Internet, prêter, distribuer et vendre des thèses partout dans le monde, à des fins commerciales ou autres, sur support microforme, papier, électronique et/ou autres formats.

L'auteur conserve la propriété du droit d'auteur et des droits moraux qui protège cette thèse. Ni la thèse ni des extraits substantiels de celle-ci ne doivent être imprimés ou autrement reproduits sans son autorisation.

In compliance with the Canadian Privacy Act some supporting forms may have been removed from this thesis.

While these forms may be included in the document page count, their removal does not represent any loss of content from the thesis.

Conformément à la loi canadienne sur la protection de la vie privée, quelques formulaires secondaires ont été enlevés de cette thèse.

Bien que ces formulaires aient inclus dans la pagination, il n'y aura aucun contenu manquant.

Canada

RAMAN SPECTRA OF THE B MODE OF THE FERROELASTIC COMPOUND $Rb_4LiH_3(SO_4)_4$ AS A FUNCTION OF TEMPERATURE

by

© Oktay Aktas
B.Sc. in Physics

A thesis submitted to the
School of Graduate Studies
in partial fulfillment of the
requirements for the degree of
Master of Science.

Department of Physics and Physical Oceanography
Memorial University of Newfoundland

September 8, 2008

ST. JOHN'S NEWFOUNDLAND

Contents

Abstract

Raman scattering measurements were performed on the ferroelastic compound $Rb_4LiH_3(SO_4)_4$ to determine whether the phase transition at $T_c = 132$ K is proper or pseudoproper ferroelastic. A double grating spectrometer was used to measure the frequency of the Raman active B mode at 31 cm^{-1} in $Rb_4LiH_3(SO_4)_4$ as a function of temperature using two different scattering geometries. Right-angle measurements were performed between 20 K and 295 K whereas the temperature range for back scattering measurements was from 60 K up to 285 K.

Our Raman measurements reveal that the square of the frequency of the optical B mode at 31 cm^{-1} shows two linear temperature dependencies corresponding to temperatures above and below T_c. This behavior has been analyzed using a pseudoproper ferroelastic Landau Model which accounts well for the temperature dependence of a soft optical mode. Our Raman investigation clearly indicates that the nature of the ferroelastic phase transition in $Rb_4LiH_3(SO_4)_4$ is pseudoproper ferroelastic.

Acknowledgments

I would like to express my sincere appreciation and gratitude to my supervisors Dr. Maynard J. Clouter and Dr. Guy Quirion for their support, guidance, and helpful discussions. I would like to thank them for reading the drafts of my thesis, and suggestions for its improvement. I am also grateful to Dr. Clouter for teaching me scattering measurements, and cryogenic system. His devotion to science has stimulated me a lot in the long path to being an experimental physicist.

I am grateful to Marek Bromberek for the helpful discussions about Landau Theory and Raman scattering, and for teaching me sample preparation. It would not have been easy to adjust to my new work place without his help. My special thanks go to Gordon Whelan for making equipment for Raman and Laue diffraction setups. I also would like to thank Fred Perry for assisting me with software problems. I learned more about physics thanks to my instructors Dr. S. Curnoe, Dr. K. Poduska, and Dr. J. Lewis. I would like to thank my classmates, too, for helpful discussions about the coursework.

I wish to thank my parents and brother for their support and guidance. I dedicate this thesis to them.

List of Tables

List of Figures

Chapter 1

INTRODUCTION

Ferroelastic compounds can be defined as materials in which uniaxial stress can be applied to switch the orientation of the structural domains which are normally present in the low symmetry phase. [1]. Ferroelastics are a type of primary ferroic materials which undergo a phase transition resulting in a group-subgroup symmetry change. Other primary ferroics are ferromagnetics, and ferroelectrics [2]. In a ferromagnetic crystal, the phase transition is accompanied by the onset of spontaneous magnetization which results in magnetic domains in the low symmetry phase. Similarly, a ferroelectric crystal undergoes a phase transition accompanied by the emergence of spontaneous polarization. Ferroelastics are mechanical analogs of ferroelectrics and ferromagnetics. Spontaneous strains emerge in the low symmetry phase with the apparition of at least two ferroelastic domains. A suitably oriented uniaxial stress can be applied to switch the orientation of these states in order to obtain single domain crystals. Thus, the stress-strain hysteresis is one of the fundamental characteristics of ferroelastics [3, 2].

Ferroelastics have been researched over 100 years due to their current and potential applications. Some of these applications are based on the existence of domains and their switchability. By using the switchability of ferroelastic domains, periodically spaced domains can be used as tunable optical gratings [4]. Moreover, most shape-memory-effect materials are ferroelastics. Some applications based on these materials are electrical and optical connectors, and heat engines resulting from the shape change during thermal cycling [2]. Other applications, based on domains and their switchability, include micropositioners with a memory, tailored domain patterns for resonator applications, variable acoustic delay lines, and focusing acoustic transducers [2]. Other applications exploit the characteristics of the ferroelastic phase transitions [2]. The best known example of these materials is zirconia (ZrO_2) which is an important refractory material. Zirconia goes into a ferroelastic phase transition at 1123 K from the tetragonal to the monoclinic structure [4]. The phase transition can be used to increase the strength and the fracture-toughness of the material. The material undergoes a phase transition to the monoclinic phase in order to resist the propagation of a crack. The volume increase at the phase transition forms small cracks in front of the larger crack, thus, leading to an increased absorption of internal stress [4]. Finally, ferroelastics have applications based on the coupling between strains and other physical properties. One of them is acousto-optic modulators. The propagation of an ultrasonic strain in a crystal modulates the refractive index of the material, serving as an optical grating. Both amplitude modulation and frequency translation can be achieved in this way [2].

$Rb_4LiH_3(SO_4)_4$ (hereafter referred to as RLHS) belongs to the family of crystals $A_4LiH_3(BO_4)_4$, where $A = Rb, NH_4, K$, and $B = S, Se$. Almost all crystals in this family undergo a structural phase transition from the tetragonal point group 4 to the monoclinic point group 2. Apart from $K_4LiH_3(SO_4)_4$, and $K_4LiH_3(SeO_4)_4$, ferroelasticity in $Rb_4LiH_3(SO_4)_4$ [12], $Rb_4LiH_3(SeO_4)_4$ [6], $(NH_4)_4LiH_3(SO_4)_4$ [7], $(NH_4)_4LiH_3(SeO_4)_4$ [7] has been confirmed by various groups. Ferroelastic domain walls in these crystals were found to be mutually perpendicular lying in the x-y plane [8, 9, 10]. In particular, the ferroelastic domain structure of RLHS has been observed using a polarizing microscope which shows two mutually perpendicular walls rotated about the z-axis by about 35° away from the x-axis. Although there have been many investigations on RLHS regarding its structural and elastic properties, some of the experimental results are not fully consistent.

The chemical formula of RLHS was initially designated as $LiRb_5(SO_4)_2 \cdot 1.5\ H_2SO_4$ [5, 11, 12]. However, the measured density value calculated from x-ray data led to the chemical formula $Rb_4LiH_3(SO_4)_4$ [13]. Another controversy about RLHS was its structure above and below the ferroelastic phase transition at $T_c = 132$ K. Initially, Brillouin scattering measurements suggested that the transition is $4mm \rightharpoonup mm2$ [11]. However, x-ray investigations by Zuńiga et. al. [14] showed that RLHS in the high symmetry (HS) (paraelastic, prototype) phase consisted of 87 % of laevorotatory crystal in the space group $P4_1$, and 13 % of dextrorotatory crystal in the space group $P4_3$. Mróz et. al. (1997) [8] conducted neutron diffraction experiments on RLHS to confirm its structure. However, the fit for the atomic positions from the neutron diffraction data indicated that the structure in the HS phase is a single phase with the space group $P4_1$, denying the existence of the phase with the space group $P4_3$. Attempts to determine the low symmetry (LS) (ferroelastic, daughter) phase was also made [8, 14], and they finally concluded that the LS phase belongs to the monoclinic space group $P2_1$. This is in agreement with the theory of structural phase transitions [15, 16]. It requires that the ferroelastic phase transition from the tetragonal point group 4 must be to the monoclinic point group 2.

As previously discussed, the ferroelastic phase transition is accompanied by the emergence of spontaneous strains. According to Tolédano [15, 17], the spontaneous strains associated with a $4 \rightharpoonup 2$ ferroelastic phase transition should be $e_1 - e_2$ and e_6 (using Voigt notation). In this case, one expects to observe softening of the elastic constants associated with these strains, namely, $C_{11} - C_{12}$ and C_{66}. The partial softening of the elastic constant combination $C_{11} - C_{12}$ was observed by the inverted torsional pendulum method [12] and Brillouin scattering measurements [13]. Ultrasonic velocity measurements also showed partial softening of the elastic constant $C_{11} - C_{12}$ while C_{66} showed a weak temperature dependence [19, 20].

The order of the ferroelastic phase transition was also studied by various groups. Changes in the specific heat [5] and thermal expansion [18], as well as the lack of latent heat and thermal hysteresis [5] showed that the transition at $T_c = 132$ K is second order. Based on all these observations regarding the ferroelastic phase transition in RLHS, several Landau models were proposed. These models can be divided into two classes. One assumes that the driving mechanism for the phase transition is the spontaneous strains acting as the order parameter of the Landau free energy. In this case, the transition corresponds to a proper ferroelastic phase transition [13, 18, 19]. The other class of models assumes that the order parameter is another physical quantity with the same symmetry as the spontaneous strains $e_1 - e_2$ and e_6 [11, 19]. In that case, the transition is a pseudoproper ferroelastic phase transition. As examples of both classes, models proposed by Quirion et. al. [19] can be given. They investigated the temperature and pressure behavior of acoustic phonons by ultrasonic velocity measurements. In order to clarify the driving mechanism for the phase transition, they proposed a proper and a pseudoproper ferroelastic Landau model. On the one hand, the pseudoproper model quantitatively agree with the temperature and pressure dependence of the elastic constants, the pressure dependence of T_c, and the thermal expansion. On the other hand, the agreement with the proper ferroelastic model predictions is not as good. Consequently, their analysis suggests that the nature of the ferroelastic transition in RLHS is rather pseudoproper. Within the framework of the pseudoproper ferroelastic model, Quirion et. al. [19] also indicate that the Raman active B symmetry mode should act as the primary order parameter. This suggestion is supported by experimental observations obtained on another ferroelastic compound $BiVO_4$ which shows elastic properties similar to those of RLHS, and undergoes a $4/m \rightharpoonup 2/m$ pseudoproper ferroelastic phase transition. Raman measurements on $BiVO_4$ show softening of the B_g symmetry optical mode [22]. Moreover, the elastic properties of $BiVO_4$ was analyzed by David et. al. [23] within the framework of a pseudoproper ferroelastic model predictions which agree well with the experimental observations.

To our knowledge, there have been three Raman scattering investigations on RLHS. Baran et. al. [24] investigated the lattice and the molecular vibrations at room temperature, and analyzed the spectra to determine the vibrational properties of long hydrogen bonds and sulphate groups. Marchewka et. al. [25] analyzed the position of the Raman bands corresponding to hydrogen bonds above and below the phase transition temperature T_c. Finally, Mróz et. al. [26] studied the lattice vibrations of RLHS as a function of temperature. According to these measurements, the optical B mode at 31 cm^{-1} (ν_2 mode) shows softening above $T_c = 132$ K. However, they did not collect sufficient data below T_c in order to see the temperature behavior of the optic mode.

The aim of this project is to perform Raman scattering measurements on RLHS as a function of temperature in order to see the temperature behavior of the optical B symmetry ν_2 mode (at 31 cm^{-1}) above and below T_c. These measurements will enable us to clarify the true nature of the phase transition at $T_c = 132$ K, and determine whether the transition in RLHS is of proper or peudoproper ferroelastic type. Right angle scattering measurements were performed over the temperature range 20-295 K. In this geometry, the temperature dependence of the optical B symmetry ν_1, ν_2, ν_3 and ν_4 modes with frequency 15, 31, 48, and 62 cm^{-1}, respectively, are also observed. In the back scattering measurements, however, the frequency range is chosen to focus on the ν_2 mode with a large photon collection time.

This thesis is divided into 6 chapters including the first chapter as the introduction. Chapter 2 explains the Raman effect, Raman tensors, and the relation between the polarization and the intensity of the incident and the scattered light. Chapter 3 describes the experimental setup for the X-ray diffraction and Raman scattering measurements. In Chapter 4, phase transitions, and Landau theory are discussed. A Landau model for a pseudoproper ferroelastic phase transition predicting the temperature dependence of a soft optical mode is presented. Chapter 5 gives the results of right-angle and back scattering Raman measurements on RLHS performed in the temperature range from 290 to 20 K, and from 285 to 60 K, respectively with an analysis based on the pseudoproper ferroelastic Landau model. Finally, a conclusion is given in Chapter 6.

Chapter 2

RAMAN SPECTROSCOPY

This chapter is divided into three sections. In the first section, the classical and the quantum mechanical pictures of Raman scattering are discussed. In the second section, the selection rules for Raman scattering are explained based on the Raman tensors, which relate the polarization of the incident and the scattered light. Finally, the intensity of the Raman lines observed in the spectra is given in terms of the elements of the Raman tensors.

2.1 Raman Scattering

Raman Scattering is one of many processes which results from the interaction of electromagnetic radiation with matter. When a light beam is incident on a crystal, most of the incident radiation is elastically scattered from the crystal in all directions, a process which is called Rayleigh scattering. However, a very small fraction of the incident radiation is inelastically scattered by the creation or annihilation of an optical lattice vibration, which is called the Raman effect, or Raman scattering. If the angular frequencies of the incident light wave and that of the optical lattice vibration involved in the process are ω and Ω, respectively, the frequency of the scattered light ω_s due to Raman effect can be written as

$$\omega_s = \omega \pm \Omega \tag{2.1}$$

The frequency of the scattered light $\omega_s = \omega - \Omega$, associated with the creation of an optical lattice vibration, is referred as the Stokes scattering, while that with annihilation of an optical lattice vibration with frequency $\omega_s = \omega + \Omega$ is called the anti-Stokes scattering.

Raman scattering occurs due to a change in molecular polarizability induced by optical lattice vibrations. If the second rank tensor α represents the polarizability associated with an optical lattice vibration mode Ω, we normally assume that its components α_{ij} can be expanded in terms of the vibrational coordinate q_n about the equilibrium value $q_n = 0$

$$\alpha_{ij} = \alpha_{ij}^o + \left(\frac{\partial \alpha_{ij}}{\partial q_n}\right)_0 q_n \tag{2.2}$$

where

$$q_n = q_n^o \cos \Omega t. \tag{2.3}$$

If the electric field of the incident beam is a time varying function with angular frequency ω

$$\mathbf{E} = \mathbf{E_0} \cos(\omega t), \tag{2.4}$$

the induced dipole moment is then defined as

$$\begin{bmatrix} p_x \\ p_y \\ p_z \end{bmatrix} = \begin{bmatrix} \alpha_{xx} & \alpha_{xy} & \alpha_{xz} \\ \alpha_{yx} & \alpha_{yy} & \alpha_{yz} \\ \alpha_{zx} & \alpha_{zy} & \alpha_{zz} \end{bmatrix} \begin{bmatrix} E_x \\ E_y \\ E_z \end{bmatrix} \tag{2.5}$$

Substituting Eqs. 2.2, 2.3, and 2.4 in Eq. 2.5, the induced oscillating dipole moment is

$$p_i(t) = \alpha_{ij}^o E_j^o \cos(wt) + \left(\frac{\partial \alpha_{ij}}{\partial q_n}\right)_0 q_n E_j^o \cos(\Omega t) \cos(\omega t) \tag{2.6}$$

Using the trigonometric relations

$$\cos(x \mp y) = \cos(x)\cos(y) \pm \sin(x)\sin(y), \tag{2.7}$$

the induced dipole moment $p_i(t)$ takes its final form

$$p_i = \alpha_{ij}^o E_j^o \cos(\omega t) + \frac{1}{2}\left(\frac{\partial \alpha_{ij}}{\partial q_n}\right)_0 q_n E_j^o \cos(\omega - \Omega)t + \frac{1}{2}\left(\frac{\partial \alpha_{ij}}{\partial q_n}\right)_0 q_n E_j^o \cos(\omega + \Omega)t \quad (2.8)$$

Here, the first term corresponds to an oscillating dipole which gives rise to Rayleigh scattering as the frequency of the scattered light ω is the same as that of the incident light. Thus, only the last two terms correspond to Raman scattering as the frequency of the scattered light differs from that of the incident light. The frequency shift relative to the frequency of the incident electromagnetic wave can be used to measure the frequency of lattice vibration modes present in a compound. Modes observed at $\omega - \Omega$ are called Raman Stokes modes, while modes at $\omega + \Omega$ are called Raman Anti-Stokes modes. As seen in Eq. 2.8, a lattice vibration is Raman active only if at least one element of the derivative of the polarizability tensor is non-zero, i.e., $\left(\frac{\partial \alpha_{ij}}{\partial q_n}\right)_0 \neq 0$. Moreover, the intensity of Raman lines is proportional to the square of the polarizability derivatives with respect to the vibrational coordinate q_n [27],

$$I \propto p^2 \propto \left(\frac{\partial \alpha_{ij}}{\partial q_n}\right)_0^2 \quad (2.9)$$

Although the classical picture of Raman scattering explains well how the dipole moment is induced with the interaction of electromagnetic radiation with matter, it cannot explain the difference between the intensity of Stokes, and anti-Stokes processes. In the classical picture of Raman scattering, the intensity of the Stokes and the anti-Stokes scattering lines are the same. However, the intensity of the Stokes lines are always larger than that of the anti-Stokes lines, which is the breakdown of the classical picture of Raman scattering.

Quantum mechanical picture of Raman scattering explains the observed difference in the intensities of the Stokes and the anti-Stokes lines. In the quantum mechanical view, Raman scattering is the interaction of light with matter which results in the annihilation or the creation of lattice vibrations (phonons) by photons. The diagram in Fig. 2.1 describes the transitions in Raman scattering. The electronic ground state is assumed to have several vibrational states with levels designated by $n = 0, 1, 2, 3$. Excitation of the molecule by the incident photon raises the molecule from its ground sate (n = 0) of frequency ν_{00} to a virtual electronic state which is shown with dashed lines. If the molecule returns to its ground state, the energy of the scattered photon will be equal to that of the incident photon, which corresponds to Rayleigh scattering. However, if the molecule energy goes down to the excited vibrational state (n = 1) of frequency ν_{01}, the incident photon loses an energy equal to the energy difference between the ground and the excited (n = 1) states, $h(\nu_{01} - \nu_{00})$ (Raman Stokes process). In Raman anti-Stokes scattering, incident photon raises the molecule from the excited vibrational state (n = 1) to the higher virtual state. Then, the molecule goes down to the ground state and the energy of the scattered light equals to that of the incident light plus the energy difference between the ground and the excited vibrational states. If the excited vibrational state is a real electronic state, then the scattering is called resonance Raman scattering. In normal Raman scattering, the excitation source is chosen so that the energy of the incident light is much lower than the energy of the first electronic excited state (with $E = h\nu_{11}$) [28].

According to the Boltzman law, most of the molecules will be in the ground state, the lowest energy level (n = 0). If we designate the number of molecules in this level as N_0, the number of molecules at a higher energy level (n = 1) is given by [27]

$$N_{h\nu_{01}} = N_0 e^{-\frac{h\nu_{01}}{k_B T}} \tag{2.10}$$

where k_B is the Boltzman constant, and T is the temperature. Hence, at low temperatures, the intensity of the Stokes lines is normally larger than that of the anti-Stokes counter part. The ratio of anti-Stokes to Stokes intensity is given by [29]

$$\frac{I^{anti-St}}{I^{St}} = \frac{(\nu_0 + \nu)^4}{(\nu_0 - \nu)^4} \exp^{\frac{-h\nu}{k_B T}} \tag{2.11}$$

where ν_0 is the frequency of the incident light, and ν is the frequency of the molecular vibrations. According to this result, the relative intensity rapidly decreases as the temperature

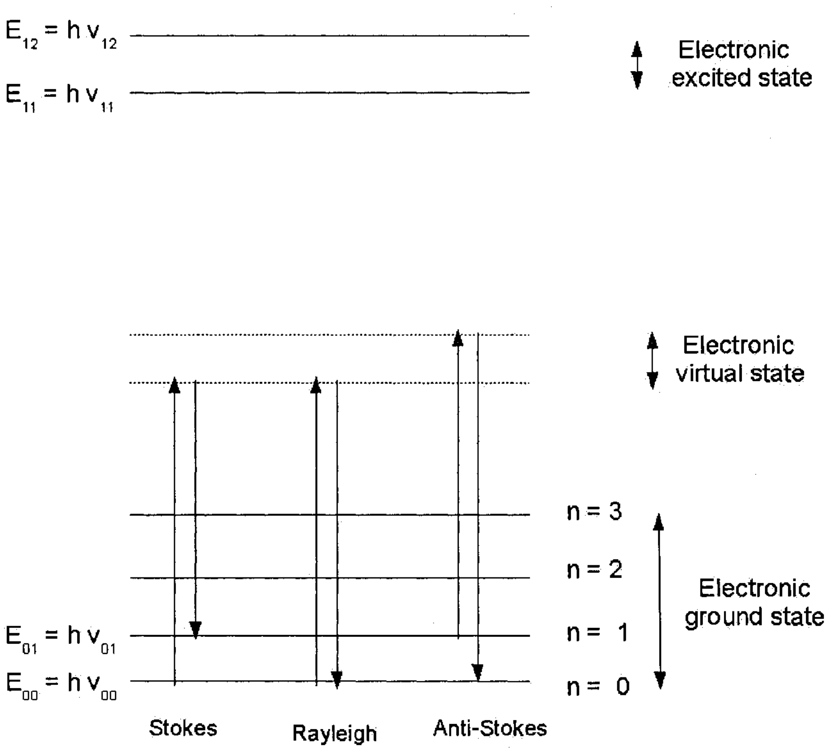

Figure 2.1: A schematic diagram of vibrational transitions for Raman and Rayleigh Scatterings

approaches zero due to the Boltzman factor. For that reason, as both lines give the same information, the Stokes lines are usually preferred to the anti-Stokes lines.

2.2 Polarizability and Raman Tensor

As mentioned earlier, a vibrational transition is Raman active, if at least one element of the derivatives of the polarizability tensor, called the Raman tensor [4], is non-zero. The Raman tensors relate the electric fields of the incident and the scattered light for a given phonon mode. This relation can be expressed as [30]

$$\begin{bmatrix} E_x^s \\ E_y^s \\ E_z^s \end{bmatrix} = \begin{bmatrix} a_{xx} & a_{xy} & a_{xz} \\ a_{yx} & a_{yy} & a_{yz} \\ a_{zx} & a_{zy} & a_{zz} \end{bmatrix} \begin{bmatrix} E_x^i \\ E_y^i \\ E_z^i \end{bmatrix} \tag{2.12}$$

where E_x^s, E_y^s, and E_z^s are the components of the electric field of the scattered light along the x, y, and z axis, and E_x^i, E_y^i, and E_z^i are the electric field components of the incident light. Hence, if the element of the Raman tensor α_{ij} is non-zero, Raman scattering is possible between the electric fields E_i^s and E_j^i.

Raman tensors are given according to the symmetry species of the crystallographic point groups [31, 32]. These symmetry species, denoted by A, B, E and F label the irreducible representations of the point groups. Certain properties of molecules such as vibrational (phonon) modes may behave differently under the symmetry operations of its point group. This behavior is described by these irreducible representations given in character tables which are specific for each point group [32]. A species of vibration in a molecule belongs to the certain irreducible representation if it changes under symmetry operations exactly as it is specified for this irreducible representation. The species of vibration is represented by A if the transformation of the molecule is symmetric with respect to the rotation about the principle axis of symmetry, whereas, it is designated by B if it is anti-symmetric [28]. A and B are one dimensional, non-degenerate representations. E and F, on the other hand, correspond to two and three dimensional, degenerate vibrations, respectively [28]. As a result, Raman tensors make it possible to determine the symmetry species of a phonon mode. In this section, we present the Raman tensors for the tetragonal point group 4 and monoclinic point group 2 as RLHS belongs to these point groups above and below the ferroelastic phase transition, respectively. Raman tensors for the tetragonal point group 4 [31, 32] are

$$\mathrm{A}:\frac{\partial\alpha}{\partial \mathrm{q}_{\mathrm{A}}}=\begin{bmatrix} a & 0 & 0 \\ 0 & b & 0 \\ 0 & 0 & c \end{bmatrix},\ \mathrm{B}:\frac{\partial\alpha}{\partial \mathrm{q}_{\mathrm{B}}}=\begin{bmatrix} c & d & 0 \\ d & -c & 0 \\ 0 & 0 & 0 \end{bmatrix} \tag{2.13}$$

$$\mathrm{E(x)}:\frac{\partial\alpha}{\partial \mathrm{q}_{\mathrm{E(x)}}}=\begin{bmatrix} 0 & 0 & e \\ 0 & 0 & f \\ e & f & 0 \end{bmatrix},\ \mathrm{E(y)}:\frac{\partial\alpha}{\partial \mathrm{q}_{\mathrm{E(y)}}}=\begin{bmatrix} 0 & 0 & -f \\ 0 & 0 & +e \\ -f & e & 0 \end{bmatrix} \tag{2.14}$$

and the Raman tensors for the monoclinic point group 2 [32] are

$$\mathrm{A}:\frac{\partial\alpha}{\partial \mathrm{q}_{\mathrm{A}}}=\begin{bmatrix} a & d & 0 \\ d & b & 0 \\ 0 & 0 & c \end{bmatrix},\ \mathrm{B}:\frac{\partial\alpha}{\partial \mathrm{q}_{\mathrm{B}}}=\begin{bmatrix} 0 & 0 & e \\ 0 & 0 & f \\ e & f & 0 \end{bmatrix} \tag{2.15}$$

where q_i are the normal coordinates which transform like the irreducible representation given by the subscript i.

We will clarify these Raman tensors by using the tensors of the tetragonal phase of RLHS in Eq. 2.13. For example, using incident light polarized along the x axis, and scattered light polarized along the x axis, the observed modes may belong to A or B symmetry as both tensors have a non-zero element α_{xx}. However, if we set the polarization of the incident and the scattered light along the z axis, then we observe only the A symmetry modes (α'_{zz}), while setting the polarization of the incident and the scattered light as x, and y will enable us to observe only B symmetry modes (α'_{xy}).

Raman scattering may occur at any angle, however, right-angle scattering is most commonly used as the intensity of the Rayleigh line is weaker compared to other scattering geometries. Nevertheless, back scattering, as well as forward scattering, are also used as these geometries give information that is not always provided by right-angle scattering. For example, these two scattering geometries are especially used when one would like to observe only longitudinal or transverse modes, where the direction of phonon propagation is parallel, and perpendicular, respectively. The experimental scattering geometry is easily represented by a four letter symbol, called the Porto notation [33]: $k_i(e_ie_s)k_s$, where the k_i, and k_s are the propagation directions with respect to the crystallographic coordinate axes, and e_i, and e_s are the polarization directions of the incident and the scattered light, respectively. Another advantage of this notation is that the directions of radiation and polarization are given with respect to the crystallographic axis, which makes it easier to determine which modes are observed by the Raman measurements. The notation $y(xy)x$ indicates that the excitation light is incident on the sample along the y axis, and polarized along the x axis, while the scattered light is propagating along the x axis, and polarized along the y axis. Referring to Eq. 2.13, B symmetry modes can be observed in the HS phase of RLHS using $y(xy)x$, $z(xy)x$, $z(yx)y$, and $z(xy)\overline{z}$ scattering geometries. On the other hand, the symmetry of the Raman modes changes at the transition temperature T_c as there is a structural phase transition from the tetragonal point group 4 to the monoclinic point group 2. Considering the Raman tensors for the monoclinic phase in Eq. 2.15, it is seen that the A and B symmetry modes of the tetragonal phase become those of the A symmetry modes of the monoclinic phase while E symmetry modes become B symmetry modes in the monoclinic phase.

In our Raman scattering experiments, both back-scattering, and right-angle scattering geometries were used. In the right angle experiments, the experimental geometry $y(xy)x$ was used in order to observe only B symmetry modes. As seen in Eq. 2.9, the intensity of the observed Raman lines is proportional to the square of the associated element of the Raman tensor. In this case, the intensity of the Raman lines measured by the geometry $y(xy)x$ is proportional to d^2. When the temperature is decreased below T_c, although the observed Raman lines are A symmetry modes of the monoclinic symmetry, their intensity are determined with a combination of the tensor elements. This is because the monoclinic phase has two domains separated by two mutually perpendicular domain walls rotated by 35° around the c axis [8]. Hence, the intensity of the Raman lines in the monoclinic phase are affected by the domains depending on which domains the beam is incident on.

In the back scattering experiments, the scattering geometry was $z(sp)\overline{z}$, where s corresponds to the polarization along the [110] direction, and p corresponds to the polarization along the $[1\overline{1}0]$ direction. In this case, the Raman tensor is rotated counterclockwise by $\frac{\pi}{4}$ about the crystallographic z axis. Using the rotation matrix [34]

$$R = \begin{bmatrix} \cos(\theta) & \sin(\theta) & 0 \\ -\sin(\theta) & \cos(\theta) & 0 \\ 0 & 0 & 1 \end{bmatrix} \tag{2.16}$$

B symmetry Raman tensor in the new coordinate system with basis *spz* become

$$R\frac{\partial\alpha}{\partial q_B}R^{-1} = \begin{bmatrix} d\sin(2\theta) & -c\sin(2\theta) & 0 \\ -c\sin(2\theta) & -d\sin(2\theta) & 0 \\ 0 & 0 & 0 \end{bmatrix} \tag{2.17}$$

Substituting $\theta = \frac{\pi}{4}$, it is found that the scattering is due to the element $-c$, and the intensity of the Raman lines is proportional to c^2.

Chapter 3

EXPERIMENTAL METHODS

This chapter describes the sample preparation, determination of the crystal orientation by Laue transmission diffraction, and the set-up for Raman spectroscopy. After a brief discussion of the sample preparation, Laue transmission diffraction set-up is explained, and the resulting Laue patterns are presented. In the final section, the optical set-up for Raman spectroscopy, the double grating spectrometer and cryogenic system for low temperature experiments are described.

3.1 Sample Preparation

RLHS crystals used in the experiments were grown in the Crystal Physics Division, Faculty of Physics at Adam Mickieicz University, Poland. In order to perform Laue transmission diffraction experiments, thin slices from the samples were cut with a wire saw (South Bay Technology, model 850) and ground to a thickness of approximately 350 microns using abrasive slurry which is a mixture of glycerin, and silicon carbide grain (with a particle size of 1200 microns). The sample used for back scattering measurements had dimensions of 3-5-0.35 mm whereas those of the sample used for right angle measurements had dimensions of

2-2-4 mm. The back scattering sample is shown in Fig. 3.1. Prior to Raman scattering experiments, samples were ground and then polished with a soft piece of cloth in order to minimize surface scattering.

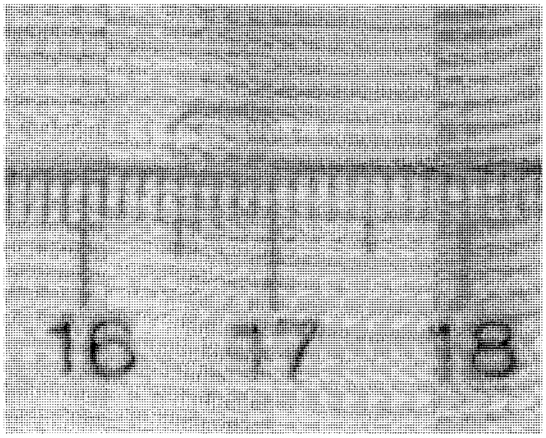

Figure 3.1: The sample for Back Scattering Measurements: The normal to the surface is the z direction.

3.2 Laue X-ray Diffraction Setup

Orientation of the samples was determined using Laue transmission diffraction experiments. An X-ray diffractometer by AFC-6R Rigaku Inc. was modified to perform Laue X-ray diffraction. X-rays were generated by a Molybdenum X-ray tube (Rigaku Inc.,Model AFC-6R). The X-ray tube operated at 50 kV and 25 mA for optimum performance.

A schematic diagram of the experimental set-up is shown in Fig. 3.2. Generated X-rays passing through the collimator were diffracted by the sample to finally generate a Laue pattern on a Polaroid film (Polaroid 57, 4*5 Instant Sheet Film loaded in Polaroid 545i 4*5 Film Holder) positioned behind the sample (suitable for transmission diffraction). A diode laser was used to align the X-ray beam, the sample, and the center of the film on the same axis (z-axis in the figure). The four circle goniometer which was previously designed for computer-controlled operation was modified to operate manually. Four knobs were connected to the stepper motors in order to manually rotate the sample around z and y axis, and to position the diode laser for alignment. Two of the knobs are seen in the figure while the other two are on the other side of the goniometer. Each experiment was run about 60-90 minutes depending on the sample thickness.

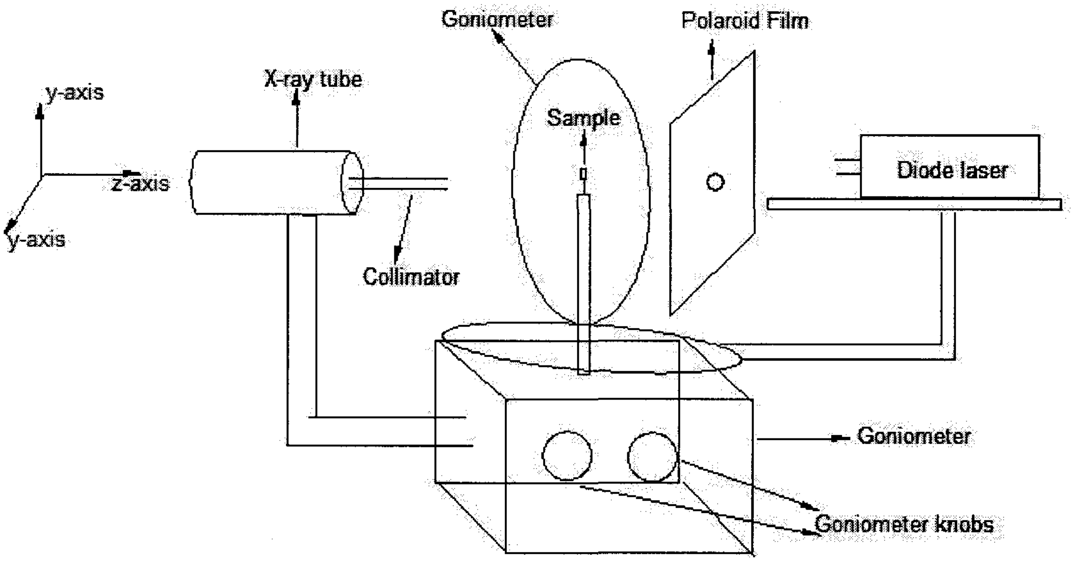

Figure 3.2: Laue Transmission Diffraction Setup

The resulting Laue diffraction patterns were compared with simulations obtained using the OrientExpress software. In order to simulate the Laue patterns with OrientExpress, the lattice parameters, the space group, the diffraction angle and the size of the polaroid film as well as the distance from the crystal to the polaroid film have to be entered. OrientExpress then calculates the coordinates of the possible diffraction spots due to specific sets of planes. It also computes the systematic absences dictated by the unit cell configuration but does not calculate the intensities of the reflections. More information on the OrientExpress software and tutorials can be found in Ref. [35]. After the determination of the crystal orientation, the samples were cut according to the desired orientation.

Before the Laue experiments were performed on the RLHS samples, a 6H-Silicon carbide crystal with known orientation was used to test the set-up. The Laue pattern is shown in Fig. 3.3. The X-rays were sent through the sample along the [110] direction, i.e., normal to the *c* axis. The expected two-fold symmetry was observed with slight distortion which is due to the difficulty of precisely aligning the sample surface perpendicular to the beam axis. Moreover, some points are missing in the Laue picture as a result of the low intensity, and slight disorientation of the normal to the sample surface.

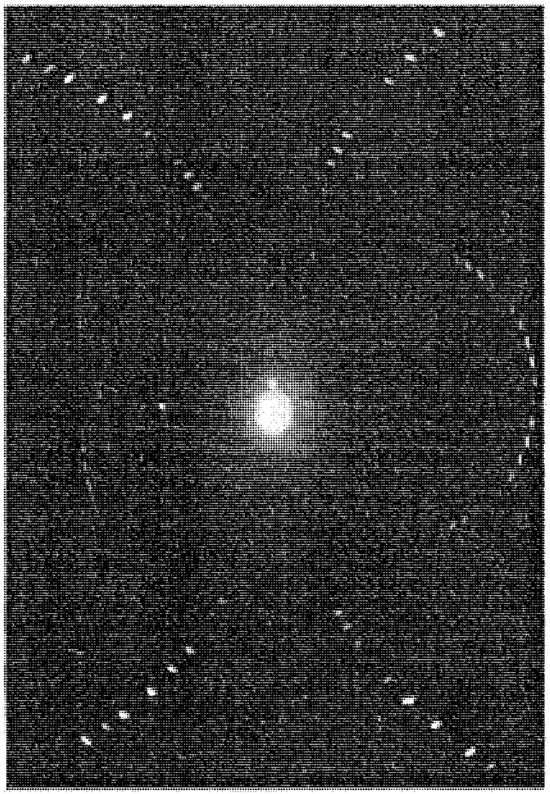

Figure 3.3: Laue pattern of 6H-SiC along the [110] direction. A two-fold symmetry is observed with slight asymmetry.

y axes forming horizontal and vertical lines. Note the number of spots in the simulation, and the experimental results. OrientExpress does not compute the intensities of the reflections, which may result in a larger number of Laue spots calculated depending on the wavelength range (0.025-0.3 nm for molybdenum x-ray source). In a real Laue pattern, as in Fig. 3.4, most of the weak reflections are not observed.

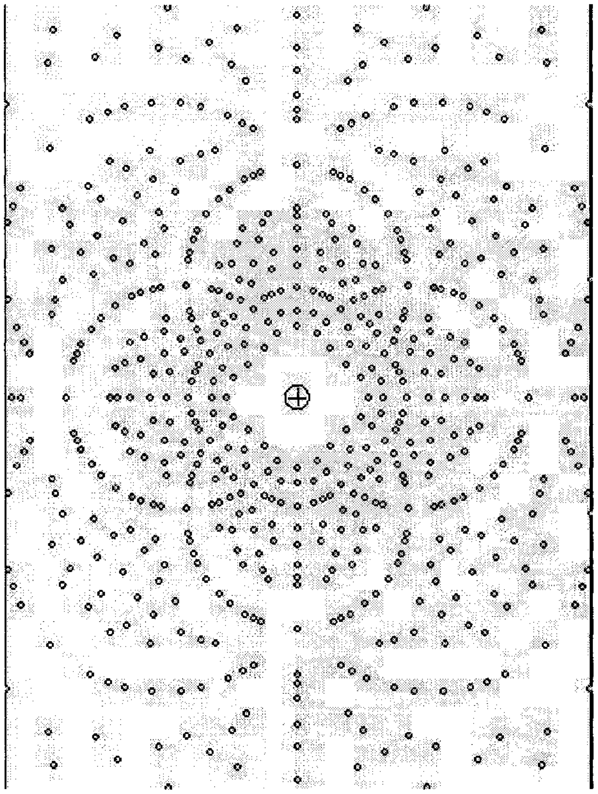

Figure 3.5: Simulation of a Laue pattern of RLHS along the z direction.

The Laue pattern obtained along the x direction is compared to the simulated pattern in Fig. 3.6. As stated before, RLHS has a 2 fold symmetry along the x and y axes which is clearly observed in the Laue pattern with the z and y axes being aligned vertically and horizontally, respectively.

Several Laue experiments were performed on the RLHS samples to confirm the crystal orientation, or to determine the x and y axes of the samples. As RLHS has a tetragonal structure, there is a four-fold symmetry along the z axis, whereas, there is a two-fold symmetry along the x and y axes. The Laue patterns shown in Fig. 3.4 were obtained with the X-ray beam parallel to the z ([001]) direction of the sample. In the first pattern on the left, the x and y axes are slightly tilted with respect to the horizontal and vertical axes, whereas they are rotated by 42° in the second pattern. Ellipses in the patterns are not exactly symmetric and of different size due to the beam axis which is not exactly perpendicular to the z-surface of the crystal.

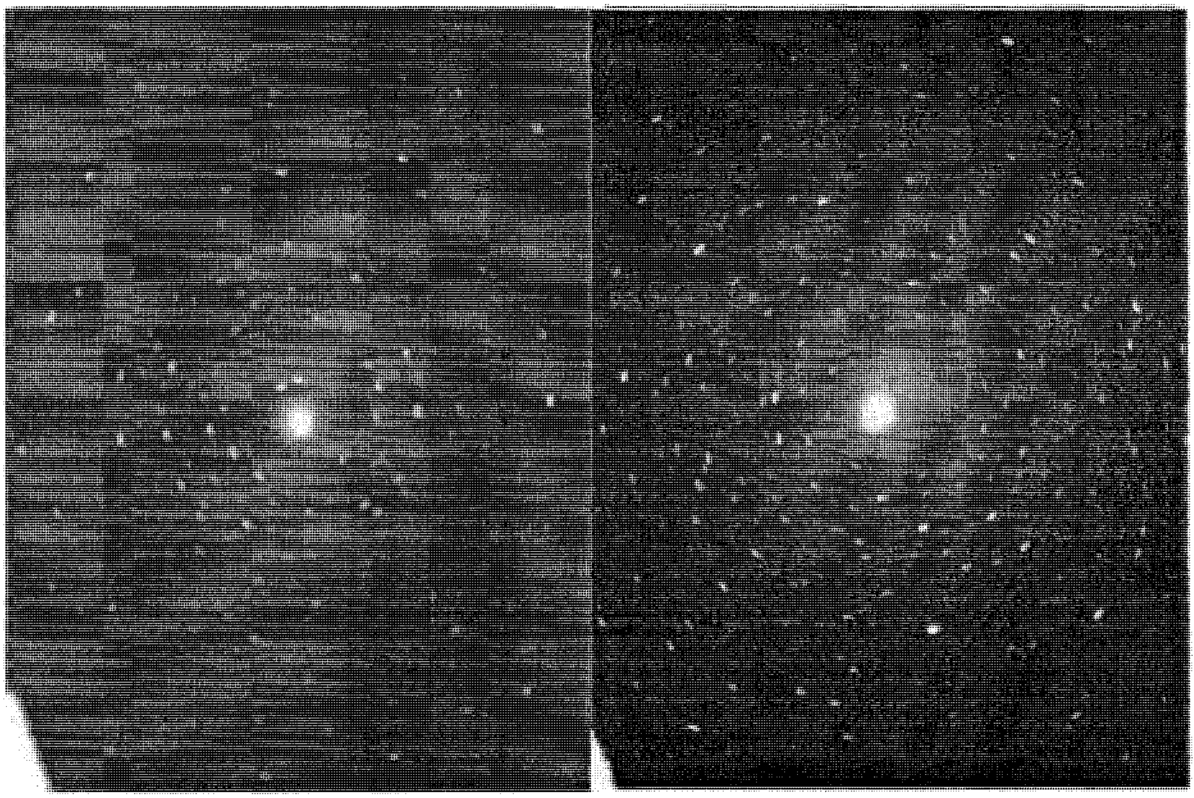

Figure 3.4: Laue patterns of RLHS along the z direction.

An ideal Laue pattern for a 4 symmetry point group is shown in Fig. 3.5 with the x and

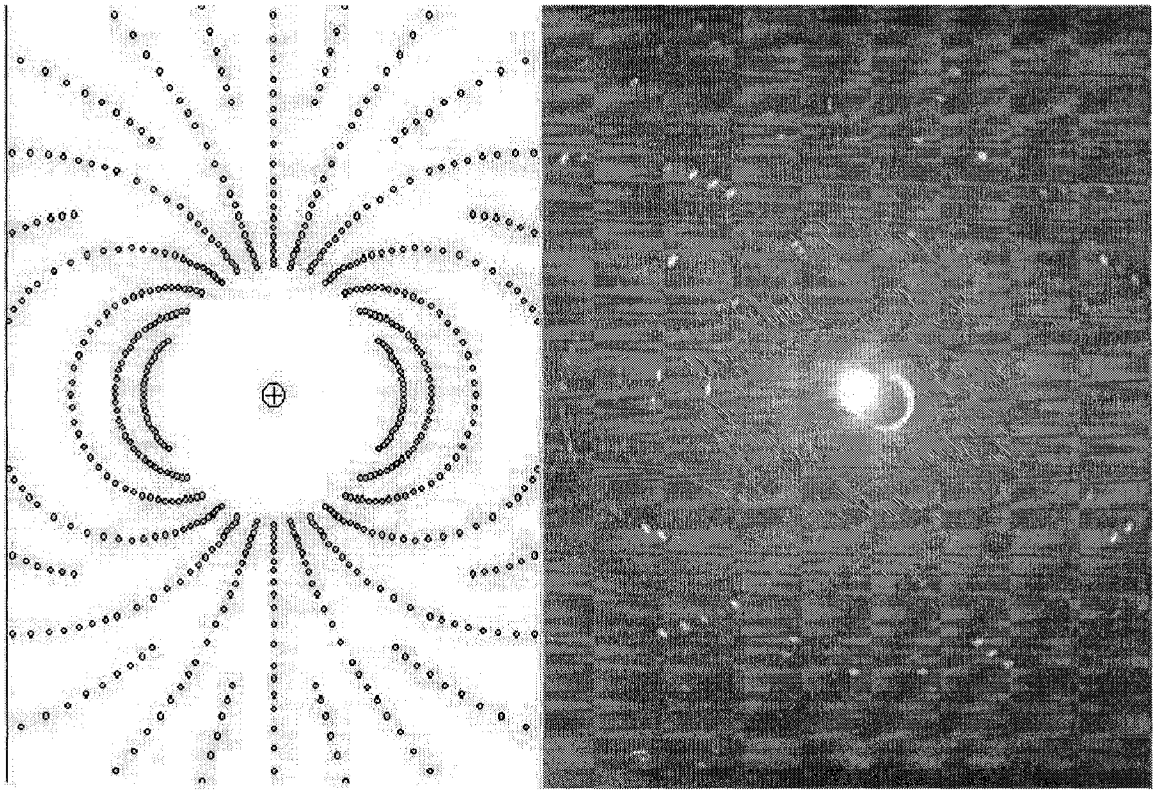

Figure 3.6: Laue pattern of RLHS along the x direction: The pattern on the left is the simulation, and the one on the right is the experimental pattern.

3.3 Set-up for Raman Spectroscopy

The laser light for Raman scattering measurements was generated by a tunable Argon-ion Laser (Spectra Physics, series 2000), which operates at a wavelength of 514.5 nm, 501.7 nm, 496.5 nm, 488.0 nm, 476.5 nm, 472.9 nm, 465.8 nm, or 457.9 nm. The wavelength of the output light was set to 514.5 nm. The intensity of the incident light beam was adjusted using the attenuator A. The intensity for back-scattering experiments was approximately 200 mW, whereas it was adjusted to 500 mW for the right-angle scattering geometry.

The optical set-up for Raman scattering experiments is shown in Fig. 3.7. Due to the difference in geometry between back and right angle scattering experiments, the converging lens, mirrors, and the prism were positioned differently for each experiment as seen in the figure. In back scattering geometry, the light beam was reflected from the mirror M1 and directed toward the sample by the prism Pr1 before being focused by the converging lens L2. In the right angle geometry, the light beam was first focused by the lens L1, then reflected from the mirror M2, and directed toward the sample by the aluminum reflector Pr 2 which was in the cryostat. The rest of the elements of the optical set-up were the same. The beam raiser BR and the attenuator A were used to adjust the height and intensity of the incident light beam. The scattered light was collected by the lens L2 (f = 20 cm) and focused into the slit using the lens (L3, f = 40 cm). The beam splitter BS was used for visual observation of the sample through a microscope in order to accurately focus the beam on the sample surface. Polarizations of the incident and the scattered light were adjusted using the half-wave plate P1 and the polarizer P2, respectively. The crystal and the center of the two lenses were positioned at the same height as the center of the slit. The scattered light was detected using a data collection and acquisition system consisting of a double grating spectrometer (Spex Industries Inc., model 1401), a cooled-photomultiplier tube, an amplifier-discriminator, a photon counter (Princeton Applied Research, model 1109), and a computer.

3.3.1 Spectrometer

The double grating spectrometer is shown in Fig. 3.8. Incident light passing through the slit S1 is then reflected from the mirror M1. After being diffracted by the first grating G1, it is reflected from the mirrors M2 and M3 before passing through the slit S2. After being reflected from mirrors M4 and M5, the light beam is diffracted from the second grating G2. Finally, the beam is reflected by the mirror M6 and passes through the third slit S3 before reaching the photomultiplier tube. The mirrors M1, M2, M5, and M6 are concave, while

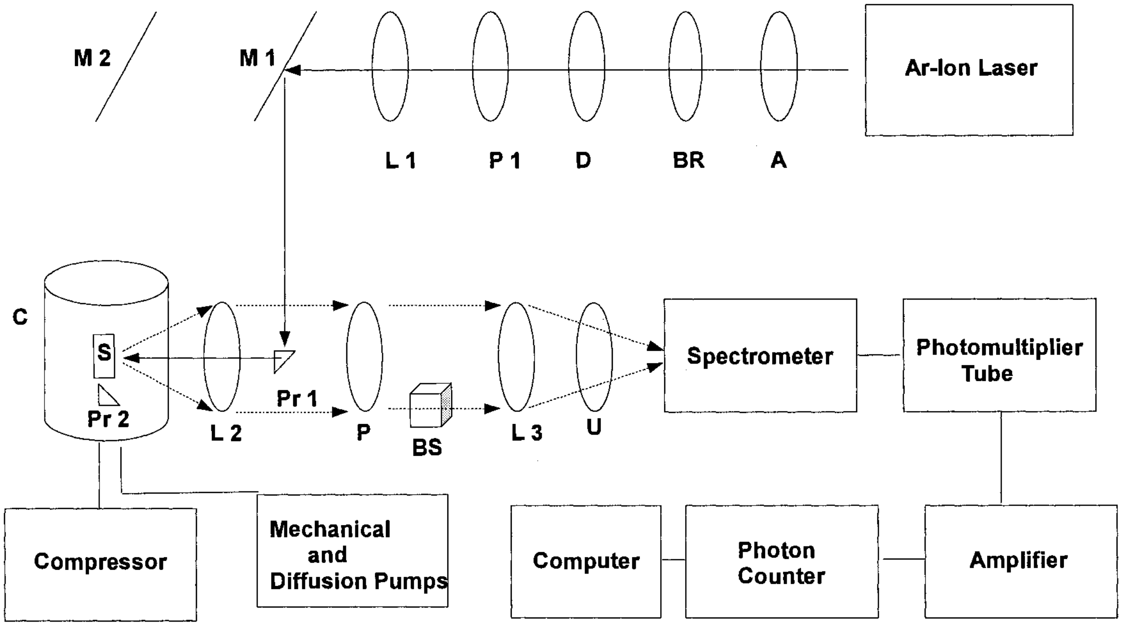

Figure 3.7: Raman Scattering Set-up for back and right angle measurements: Light path for back scattering measurements is shown in the diagram. Continuous lines with arrows represent the incident light beam whereas dashed lines refer to the scattered light. Incident beam for right-angle measurements is reflected from the mirror M2 and go through the bottom surface of the sample by the aluminum reflector Pr2, and the scattered light follows the same path as that for back scattering measurements. Refer to the text for the elements of each setup.

mirrors M3 and M4 are flat mirrors.

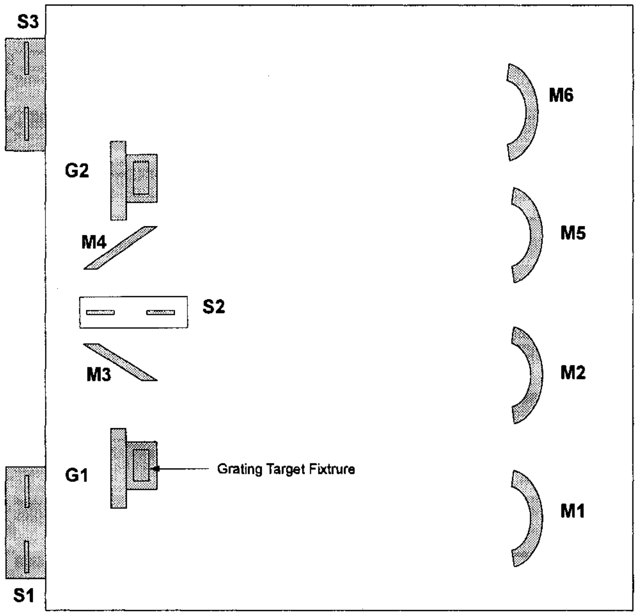

Figure 3.8: Spectrometer Diagram: Elements of the double spectrometer: M1, M2, M5, and M6 are concave mirrors; M3 and M4 are flat mirrors; S1, S2, and S3 are slits; and G1, and G2 are gratings.

The spectrometer operation is based on the fundamental grating equation

$$m\lambda = d(\sin\alpha + \sin\beta) \tag{3.1}$$

where

m = order of diffraction

λ = wavelength

d = grating spacing

α = angle of incidence

β = angle of diffraction. The resolution of the grating is given by

$$R = \frac{\lambda}{\Delta\lambda} = \frac{\nu}{\Delta\nu} = Mn, \tag{3.2}$$

where M is the total number of the grating grooves, and n is the order of diffraction. In general, this resolution is reduced by aberrations and imperfections associated with mirrors, lenses and the width of the slits. The width of the slits S1 and S3 was set to 300 microns for back scattering experiments, whereas, it was set to 200 microns for right-angle experiments. The width of the slit S2 was set to 100 microns larger than that of the slits S1 and S3. The f-number (the focal length divided by the aperture diameter) of the spectrometer is 7.8. As a result, the lens L3 was chosen to have a similar f-number (40 cm focal point, and 5 cm in diameter).

3.3.2 Cryostat

To perform experiments under vacuum in the temperature range from 20 to 300 K, a two-stage closed cycle helium refrigerator system with mechanical and diffusion pumps was used during the experiments. The system contains two units: (1) Compressor module (APD Cryogenics Inc, model HC2) and (2) Expander module (Air Products, model DE202. The compressor and the expander module are connected to each other with two pressurized gas lines.

The expander module (see Fig. 3.9) produces the refrigeration in a two-stage close-cycle system. The temperature in the first stage is approximately 80 K and is not regulated. The sample is kept in the second stage which is surrounded by a copper radiation shield[1]. The temperature in the second stage is regulated by a cryogenic temperature controller (LakeShore Cryotronics, model DTC 500). Using a silicon diode, and two resistive heaters,

---

[1] More information on how the cryogenic system functions can be found in the manuals of the expander and the compressor modules.

the temperature can be stabilized down to 18 K. The first resistive heater is located under the sample. A second resistive heater and the silicon diode, not shown in the diagram, are placed on the other side of the aluminum sample holder. In right-angle scattering experiments, an aluminum reflector, shown in the figure, is used to send the light through the bottom surface of the sample. The sample was kept under high vacuum using a diffusion pump system in order to provide thermal insulation.

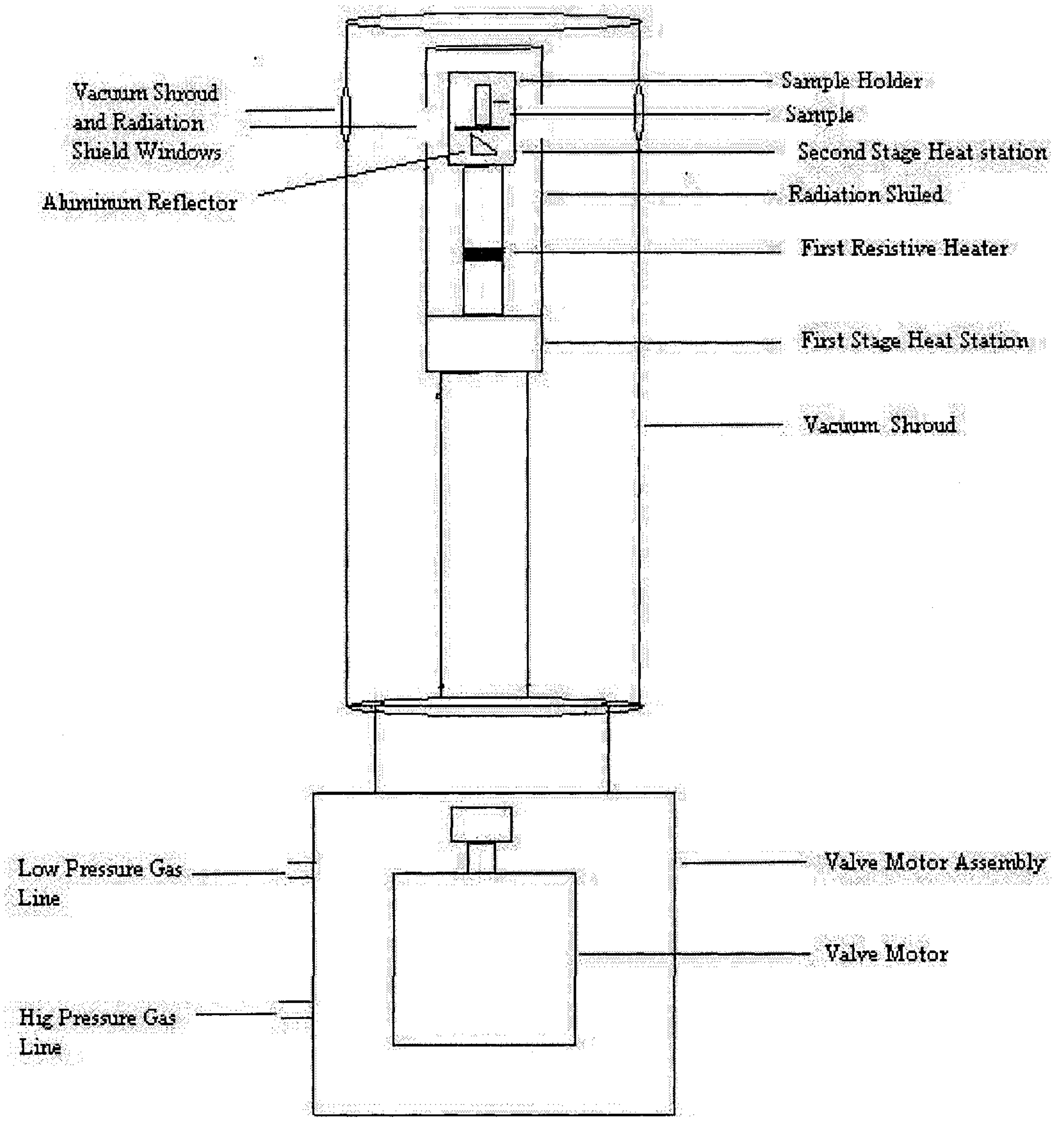

Figure 3.9: Cryostat

Chapter 4

PHASE TRANSITIONS AND LANDAU THEORY

This chapter is divided into three sections. In the first section, phase transitions are defined and classified on the basis of the Gibbs free energy formulation. Within this framework, a distinction between first and second order phase transitions is made. In the second section, Landau theory, which is primarily derived in the context of continuous phase transitions, is explained by introducing two main concepts, namely, the order parameter and the expansion of the excess Gibbs free energy in terms of that order parameter. In the third section, the expansion of a pseudoproper ferroelastic Landau model is explained. The model includes the Landau type free energy, elastic energy, and energy terms associated with the coupling between the order parameter and strains. Solutions for the temperature dependence of the order parameter, the strain, and frequency of the soft optical mode are derived.

4.1 Phase Transitions

A phase transition is the transformation of a thermodynamic system from one phase to another. A phase transition is identified when one or more physical properties of the system change abruptly as a function of an external variable such as temperature, pressure, or stress. In conformity with Ehrenfest's classification, phase transitions can be labeled on the basis of mathematical properties of the Gibbs free energy describing the thermodynamic system. A phase transition is said to be n^{th} order if derivatives of the Gibbs potential up to the $n-1$ are continuous, while the n^{th} order derivatives show discontinuities [37]. The Gibbs potential, or, the Gibbs free energy, can be defined as

$$G = U - TS + XY, \tag{4.1}$$

where U is the internal energy, T is the absolute temperature, S is the entropy, X is the general displacement (volume V, polarization p, magnetization M, or strain e) which is the result of a general force Y such as pressure P, electric field E, magnetic field H, or stress σ [38]. In the differential form, Gibbs free energy can be written as

$$dG = -SdT + XdY, \tag{4.2}$$

where the differential form of the internal energy, $dU = TdS - YdX$, is substituted. Then, the first partial derivatives of the Gibbs free energy take the form

$$-\left(\frac{dG}{dT}\right)_Y = S, \tag{4.3}$$

$$\left(\frac{dG}{dY}\right)_T = X. \tag{4.4}$$

Thus, according to the Ehrenfest classification, a phase transition is said to be first order or discontinuous, if the entropy or the generalized displacement X (volume, magnetization, etc) changes discontinuously at the transition temperature. Examples of this kind of transitions are liquid-to-gas, liquid-to-solid, and gas-to-solid phase transitions, in which the volume shows discontinuity at the transition point. Other characteristics of first order phase transitions are latent heat and thermal hysteresis.

Generally, a discontinuity in any second derivative of the Gibbs free energy implies that a second order phase transition occurs. For example, we can express two physical quantities, namely, the specific heat capacity at constant pressure C_P and the isothermal compressibility κ, in terms of the second partial derivatives of the Gibbs free energy:

$$C_p = \left(\frac{dQ}{dT}\right)_P = T\left(\frac{dS}{dT}\right)_P = -T\left(\frac{\partial^2 G}{\partial T^2}\right)_P, \tag{4.5}$$

$$\kappa = -\frac{1}{V}\left(\frac{dV}{dP}\right)_T = -\frac{1}{V}\left(\frac{\partial^2 G}{\partial P^2}\right)_T. \tag{4.6}$$

Thus, a phase transition is second order if there is a discontinuity in the specific heat capacity or isothermal compressibility. Such a phase transition is also called a continuous phase transition.

4.2 Landau Theory

Landau theory is a macroscopic thermodynamical model which describes phase transitions in which a high symmetry (HS) phase changes to a low symmetry (LS) phase. Here, the discussion will be limited to phase transitions where the symmetry of the LS phase is a subgroup of the HS group. A more general description of phase transitions can be found in Ref. [3]. Although initially derived for continuous phase transitions, it can successfully describe discontinuous phase transitions. As the phase transition in RLHS is continuous, the derivations of the physical parameters from the Landau model is limited to continuous transitions. In that context, two new characteristics need to be introduced:

- *An order parameter* Q: This parameter normally reflects the loss of some symmetry elements below the phase transition temperature T_c. Thus, its value is zero in the

HS phase, while it is non-zero below T_c. For example, the order parameter can be a departure of the atomic or electronic configuration from that of the HS phase [2].

- *Excess Gibbs Free Energy*: As the LS phase must be more stable than the HS phase below T_c, the excess Gibbs Free energy simply represents the difference between the Gibbs free energy of the LS phase G and that of the HS phase G_o [3]. This energy difference G_e is then expressed as an infinite power series of the order parameter Q such that

$$G_e = \alpha_1 Q + \frac{1}{2}\alpha_2 Q^2 + \frac{1}{3}\alpha_3 Q^3 + \frac{1}{4}\alpha_4 Q^4 + ... \tag{4.7}$$

The stable state is associated with the minimum of the G_e with respect to Q given by

$$\frac{dG}{dQ} = \alpha_1 + \alpha_2 Q + \alpha_3 Q^2 + \alpha_4 Q^3 + ... = 0, \tag{4.8}$$

Considering that $Q = 0$ in the HS phase, Eq. 4.8 can only be satisfied if $\alpha_1 = 0$. Moreover, since the phase transition in RLHS is continuous, no odd power term is allowed [3, 4], as it will result in discontinuity at the transition in the Gibbs free energy. In addition, as the value of Q is infinitesimal at temperatures close to the transition temperature, terms with a power of Q larger than 4 are normally ignored. The excess free energy G_e reduces to

$$G_e = \frac{1}{2}\alpha_2 Q^2 + \frac{1}{4}\alpha_4 Q^4. \tag{4.9}$$

Since the excess Gibbs free energy G_e corresponds to a minimum for the stable state, the first derivative of the G_e with respect to the Q must be zero, whereas its second partial derivative must be greater than zero. Taking the first and the second derivatives of Eq. 4.9 with respect to Q, we obtain

$$\frac{\partial G}{\partial Q} = \alpha_2 Q + \alpha_4 Q^3 = 0, \tag{4.10}$$

$$\frac{\partial^2 G}{\partial Q^2} = \alpha_2 + 3\alpha_4 Q^2 > 0. \tag{4.11}$$

In the HS phase, since $Q = 0$, according to Eq. 4.11 we find that α_2 must be greater than zero. However, in the LS phase with $Q \neq 0$, we find that Eq. 4.10 now imposes that α_2 must be less than zero. As α_2 must change sign, its value at the transition temperature can only be zero. Under these considerations, Landau assumed that the temperature dependence of α_2 is simply given by [39]

$$\alpha_2 = a(T - T_c) \tag{4.12}$$

where a is a positive constant. As $\alpha_2 < 0$ in the LS phase, Eq. 4.11 can only be satisfied when $\alpha_4 > 0$. The variation of G_e as a function of Q at different temperatures is illustrated in Fig. 4.1. When $T > T_c$, the equilibrium point is specified by $Q = 0$. On the other hand, the equilibrium point departs from its value $Q = 0$ at T_c to non-zero values for $T < T_c$.

Substituting α_2 in Eq. 4.10, the first derivative of G_e with respect to Q gives

$$Q = 0, \qquad T > T_c, \tag{4.13}$$

$$Q = \sqrt{\frac{a}{\alpha_4}(T_c - T)}, \qquad T < T_c. \tag{4.14}$$

with the first and second solutions corresponding to the HS and LS order parameter, respectively. The temperature dependence of the order parameter is given in Fig. 4.2. Its value changes continuously at T_c and it increases as $(T - T_c)^{0.5}$ as the temperature is decreased below T_c, which is the typical mean field result.

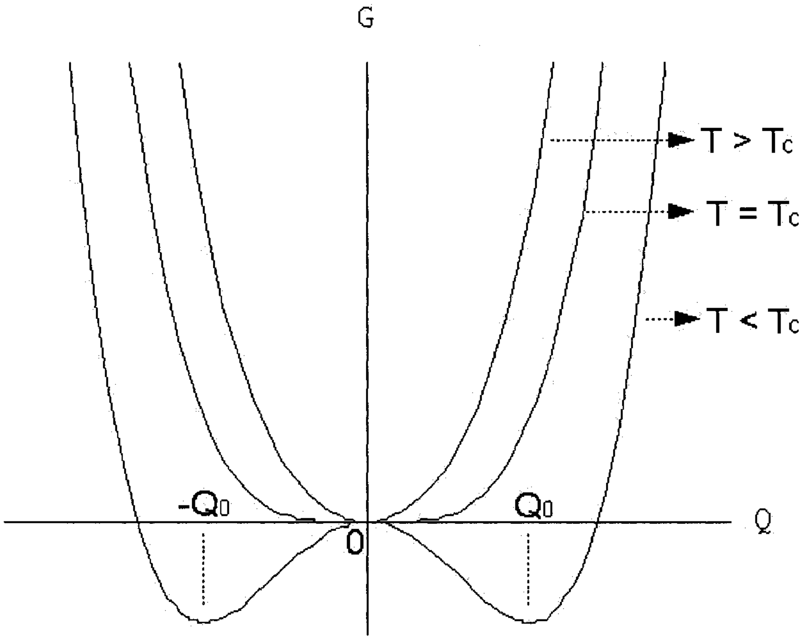

Figure 4.1: A plot of the Gibbs Free energy as a function of Q at various temperatures. At equilibrium, G_e is a parabola above T_c, and a double-well potential below T_c with equilibrium points at $Q = 0$, and $Q = \mp Q_o$, respectively.

4.3 Landau Model for a Pseudoproper Ferroelastic Phase Transition

As stated previously, RLHS undergoes a ferroelastic phase transition which results in a symmetry change from the tetragonal point group 4 to the monoclinic point group 2. As there is a group-subgroup relationship between these two point groups, a Landau model can be used to explain the elastic properties of this compound. Ferroelastic transitions have been

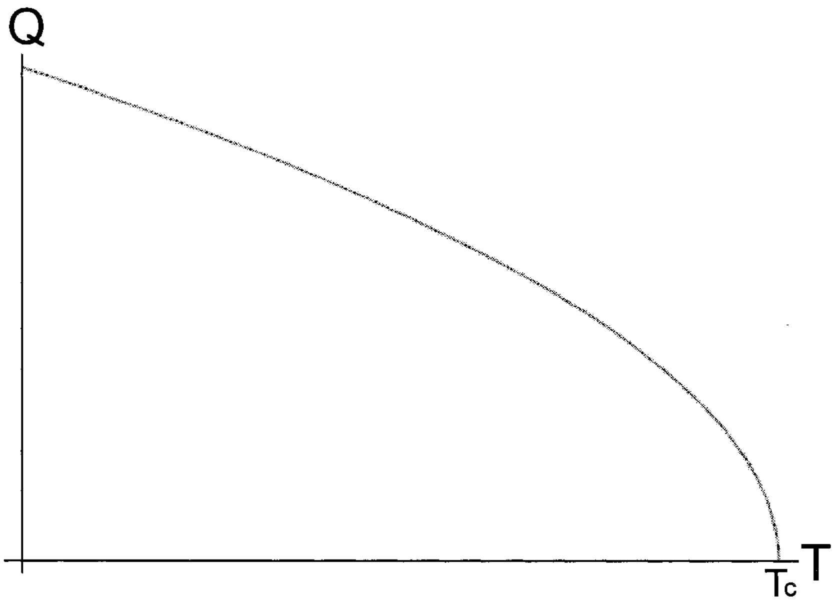

Figure 4.2: A plot of the order parameter Q as a function of temperature. The value of Q in the HS phase is 0, then it continuously increases as $\sqrt{T-T_c}$ in the LS phase.

analyzed in detail using the Landau theory by Tolédano et. al. [15, 17]. Landau theory [17] states that the order parameter Q must have the symmetry properties of the irreducible representation associated with the high symmetry phase group. According to Tolédano [17], the order parameter must belong to the one dimensional irreducible representation B (x^2-y^2, xy) of the HS phase group $P4_1$ [15, 40]. Consequently, using the function representation of the strains given in Table 4.1, we immediately note that it transforms as the spontaneous strain $e_s = (e_1 - e_2, e_6)$. As this strain combination belongs to the B irreducible representation, it can act as an order parameter and the transition can be referred as proper ferroelastic. TeO_2 [15], As_2O_5 [42], and $LiNH_4C_4H_4O_6 \cdot H_2O$ [43] are some examples of compounds which undergo a proper ferroelastic phase transition. Whenever strains are not the main order parameter, the transition is classified by Tolédano [15] as pseudo-proper ferroelastic. In this case, the order parameter Q and e_s must belong to the same irreducible representation.

A few examples of compounds undergoing a pseudoproper ferroelastic phase transition are LaP_5O_{14} [2], $KH_3(SeO_3)_2$ [21], SnO_2 [44], and $BiVO_4$ [45], where there are strong evidences that the transition is associated with softening of an optical mode.

Table 4.1: Function Representation of Strains

Strain	e_1	e_2	e_3	e_4	e_5	e_6
Function	x^2	y^2	z^2	yz	xz	xy

There has been a controversy about whether the transition in RLHS is proper or pseudoproper ferroelastic. So far, several Landau models have been put forward by several groups [13, 18, 19, 11, 19]. Some of these models claim that the transition is proper ferroelastic, assuming that the order parameter is the spontaneous strain [13, 18, 19]. Other models claim that the transition is pseudoproper ferroelastic, assuming that the order parameter is another physical quantity with the same symmetry as the spontaneous strain [11, 19]. Models by Quirion et. al. [19] can be given as examples of a proper and a pseudoproper ferroelastic model. They measured the velocity of acoustic phonons as a function of temperature and pressure and proposed these models in order to clarify the nature of the ferroelastic phase transition. The pseudoproper model quantitatively agrees with the temperature and pressure dependence of the elastic constants, the pressure dependence of T_c, and the thermal expansion. It also accounts for the temperature dependence of the acoustic mode associated with the spontaneous strain. On the other hand, the agreement with predictions based on the proper ferroelastic model is less satisfactory. Thus, their analysis leave little doubt regarding the driving mechanism for the ferroelastic transition in RLHS. Within the framework of the pseudoproper ferroelastic model, Quirion et. al. [19] also suggest that the Raman active B symmetry mode should be the primary order parameter. Previously, Mróz et. al. [26] studied the lattice vibrations of RLHS as a function of temperature. These measurements show softening of the optical B mode at 31 cm^{-1} above $T_c = 132$ K. However, they also claim that the observed softening of the B mode above T_c is insufficient to account for the pseudoproper ferroelastic phase transition compared to similar results obtained for the ferroelastic compound $BiVO_4$ [22]. Thus, further experiments are required in order to determine the temperature behavior of the B mode below T_c and results have to be reanalyzed within the framework of a pseudoproper ferroelastic model.

At last, we present a Landau model that accounts for the temperature dependence of a soft optical mode driving the pseudoproper ferroelastic phase transition. The excess Gibbs free energy G_e includes three distinct contributions from different physical mechanisms,

$$G_e = G_L + G_{el} + G_c. \tag{4.15}$$

G_L is the Landau expansion of the Gibbs free energy in terms of the order parameter given in Eq. 4.9. Here, the order parameter u represents atomic displacements associated with the soft optical mode that gives rise to optical vibrations. G_L is expressed as

$$G_L = \frac{1}{2} m {w_o}^2 u^2 + \frac{1}{2} b u^4 \tag{4.16}$$

where

$$m {w_o}^2 = a(T - T_o) = A. \tag{4.17}$$

Hence, Landau type free energy contains the temperature dependent term, where m corresponds to mass per unit volume, and w_o is the uncoupled frequency of the soft optical mode. Here, the first term $\frac{1}{2} m {w_o}^2 u^2$ represents the harmonic oscillator energy due to the optical atomic displacements. The second contribution to the excess Gibbs free energy is the elastic energy associated with elastic deformations or strains, G_{el}. For simplicity, we consider only one strain component e_s which represents an effective strain with the same symmetry as the atomic displacements u. Thus, the elastic energy G_{el} simply reduces to

$$G_{el} = \frac{1}{2} C e_s^2. \tag{4.18}$$

where C is the elastic constant. We use one strain and one elastic constant as the main purpose of this model is to derive the temperature dependence of the soft optical mode. Exact elastic energy for the tetragonal point group 4 (as a result, for RLHS) can be found in Ref. [19, 46]. As stated previously, as the order parameter u and the spontaneous strain e_s belong to the same irreducible representation, the bilinear coupling term such as

$$G_c = \gamma e_s u, \tag{4.19}$$

where γ is the coupling coefficient, must be included in the total free energy G_e. All coupling terms allowed by the symmetry for a $4 \rightharpoonup 2$ pseudoproper ferroelastic transition can be found in Ref.s [19] and [23]. Adding up all these contributions, the total free energy is

$$G_e = \frac{1}{2}mw_o{}^2u^2 + \frac{1}{2}bu^4 + \frac{1}{2}Ce_s^2 + \gamma e_s u. \tag{4.20}$$

Eq. 4.20 enables us to derive the temperature dependence of the order parameter, strain, elastic constant, and that of the frequency of the soft optical mode. Under equilibrium conditions, the excess Gibbs free energy corresponds to a minimum, which requires that

$$\frac{\partial G_e}{\partial u} = a(T - T_o)u + Bu^3 + e_s\gamma = 0, \tag{4.21}$$

$$\frac{\partial G_e}{\partial e_s} = Ce_s + \gamma u = 0. \tag{4.22}$$

Using Eq. 4.22, the spontaneous strain e_s can be expressed in terms of the order parameter u:

$$e_s = -\frac{u\gamma}{C}. \tag{4.23}$$

Substituting Eq. 4.23 in Eq. 4.21, and solving for u at $T = T_c$, we obtain

$$u = 0 \quad (HS\ Phase) \tag{4.24}$$

$$u = \frac{\sqrt{a(T_o - T + \frac{\gamma^2}{C})}}{\sqrt{B}} \quad (LS\ Phase) \tag{4.25}$$

As the order parameter must be zero at the phase transition temperature T_c, comparing Eq. 4.25 with Eq. 4.14, solving $u = 0$ for $T = T_c$ gives

$$T_c = T_o + \frac{\gamma^2}{aC}. \tag{4.26}$$

As stated previously, T_c is the temperature where the phase transition occurs, while T_o is called the stability limit which is explained later.

The frequency of the optical mode associated with the order parameter can be obtained using the equation [23]

$$m\omega^2 = \frac{\partial^2 G_e}{\partial u^2}. \tag{4.27}$$

Then, the square of the optical mode frequency above and below T_c are

$$m\omega^2 = a(T - T_c) + \frac{\gamma^2}{C}, \qquad HS\ Phase \tag{4.28}$$

$$m\omega^2 = -2a(T - T_c) + \frac{\gamma^2}{C}, \qquad LS\ Phase \tag{4.29}$$

According to this simple model, the square of the soft mode frequency ω^2 changes linearly with temperature above and below the phase transition T_c with a factor of -2 in the slope ratio. The value of w^2 reaches its minimum at T_c in the HS phase, and then increases as the temperature is further reduced in the LS phase. The stability limit T_o is described by Wadhavan [2] as the temperature at which the optical mode frequency ω would go to zero if the transition did not occur at T_c. Application of uniaxial stress on a ferroelastic compound along a suitable direction compensates the spontaneous strain, maintaining the crystal with a single domain phase below T_c. As a result, one can observe complete softening of the soft optical mode at the stability limit T_o in the absence of coupling between the spontaneous strain and the order parameter. Substituting Eq. 4.26 in Eq. 4.28 gives

$$m\omega^2 = a(T - T_o) \qquad HS\ Phase \tag{4.30}$$

For a given optical mode, T_o can be determined by extrapolation using a plot of ω^2 *vs* T.

Chapter 5

EXPERIMENTAL RESULTS AND DISCUSSION

Temperature investigations of the optical B mode at 31 cm^{-1} of RLHS were performed in order to determine whether the transition in RLHS is proper or pseudoproper ferroelastic. Two experimental scattering geometries, namely, right-angle scattering and back-scattering were used. In section 5.1, the polarized Raman spectra with right-angle scattering geometry $y(xy)x$ obtained between 295 K and 20 K are presented. In the following section, the polarized Raman spectra of the B mode with back scattering geometry $z(sp)\overline{z}$ are shown. Both sets of data have been used to determine the temperature dependence of the square of the frequency of the B mode. These new experimental data are compared with data previously obtained by Mróz et. al. [26] and analyzed within the framework of the pseudoproper ferroelastic model given in Chapter 4.

5.1 Polarized Right-Angle Raman Spectra of the B_2 Mode of RLHS

The Raman spectra of the optical B symmetry ν_2 mode (31 cm^{-1}) were taken with the right-angle geometry $y(xy)x$ in the temperature range from 295 K to 20 K. Raman B modes in the frequency range from 10 to 70 cm^{-1} were observed at room temperature and compared in Table 5.1 with those obtained by Mróz et. al. [26] and Baran et. al. [24]. The frequency of the ν_2 mode was measured to be 31 cm^{-1} in this work, while it was measured as 31 and 32 cm^{-1} by Mróz et. al. [26] and Baran et. al. [24], respectively. The ν_1, ν_3, and ν_4 modes were also observed and were found to be consistent with measurements done by other groups.

Table 5.1: Frequencies (in cm^{-1}) of the optical B symmetry modes in RLHS at room temperature (295 K)

B Modes	Current work	Mróz et. al. [26]	Baran et. al. [24]
ν_1	16	17	17
ν_2	31	31	33
ν_3	48	49	48
ν_4	62	63	62

The temperature dependence of the B symmetry ν_2 mode was investigated by lowering the temperature down to 20 K in several steps. Previous measurements realized by Mróz et. al. [26] on RLHS show that the optical B mode (ν_2) softens as the temperature is decreased down to the transition temperature $T_c = 132$ K with no sufficient data to determine the behavior below T_c. The spectra of our Raman measurements are presented in Fig. 5.1. The optical ν_1 mode at 16 cm^{-1}, whose frequency was found to be temperature independent [26], was used as the calibration line during the fittings of the spectra. In agreement with the measurements from Mróz et. al. [26], the ν_2 mode softened as the temperature was decreased down to T_c. The frequency of the ν_2 mode at T = 295 K was 30.7 cm^{-1} and decreased to 27.9 cm^{-1} at T = 134 K. When the temperature was further decreased to 20 K, the frequency increased to 30.8 cm^{-1}. The frequency of the B symmetry ν_2, ν_3, and ν_4 modes measured at different temperatures are shown in Table 5.2, and plotted in Fig. 5.2 as a function of temperature. Although the ν_3, and ν_4 modes did not show softening, their frequency varies within 1.5 cm^{-1} in the whole temperature range.

The plot of ω^2 against temperature for the B symmetry ν_2 mode is presented in Section 5.2 together with the back scattering data. The slope of the linear fit for the ω^2 vs. T graph above T_c is obtained as $s_{high} = 0.9 \pm 0.2$ while it is $s_{low} = 1.6 \pm 0.3$ below T_c. Thus, within the uncertainty, the ratio of the slopes is about -2 as expected for a pseudoproper ferroelastic transition. However, the dispersion in the LS phase results in a large uncertainty in the frequency of the ν_2 mode. In the LS phase, structural domains might be responsible for the poor quality of the spectra. As both domains lie in the xy plane, the incident and the scattered light might have to penetrate several domains, which might affect the polarization and the intensity of the scattered light. Moreover, it is known that the monoclinic angle between the x and the y axes is greater than 90° [8] although the relative angle of the polarizers was set to 90° with respect to the x axis of the tetragonal phase.

We believe that ν_1 mode of B symmetry which is used as the calibration line might show a weak temperature dependence. Considering that the softening of the B symmetry ν_2 mode is not strong (decreased by 2.8 cm^{-1} from 295 K to 134 K), a small variation in the frequency of the ν_1 mode might significantly affect the calculation for the ν_2 mode. A more precise way to measure the Stokes shift of the ν_2 mode is to use the Rayleigh line as the calibration line. As a result, we performed additional back-scattering experiments in order to see whether or not we can obtain a more precise temperature dependence.

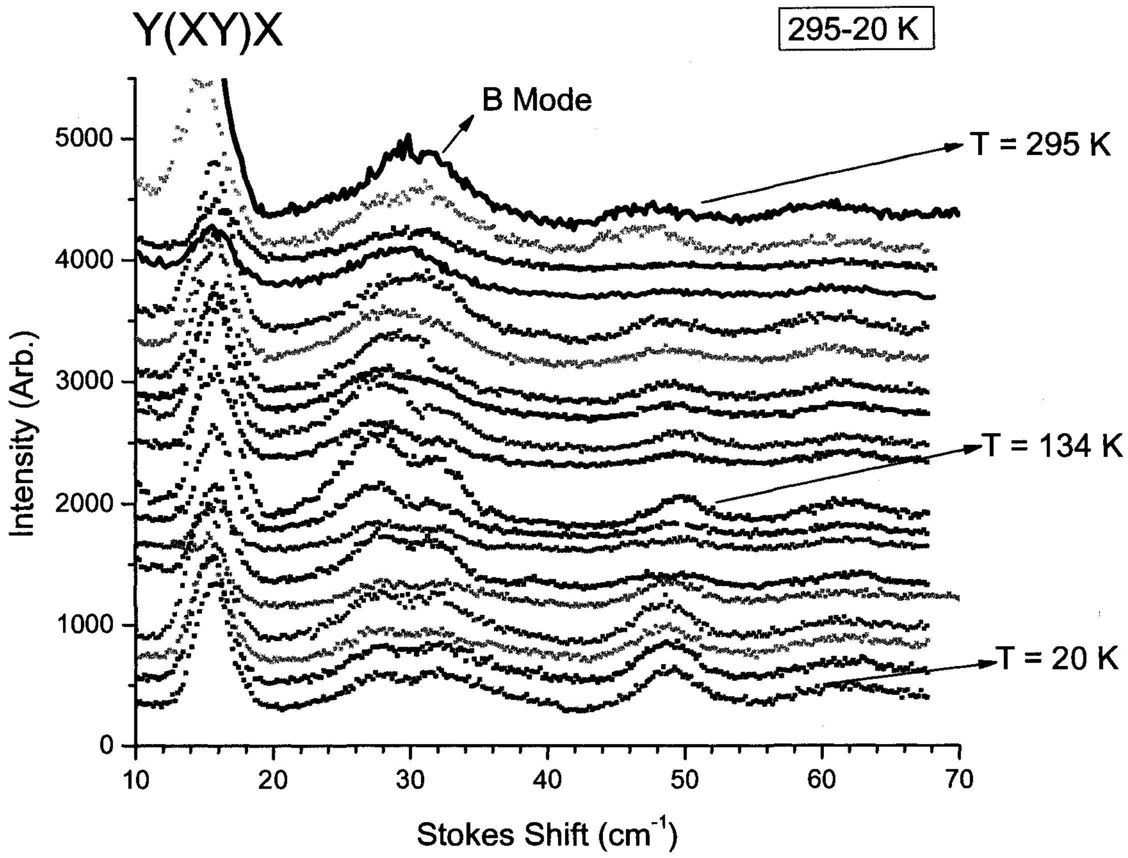

Figure 5.1: Raman Spectra of the ν_2 mode of B symmetry obtained using the right-angle scattering geometry in the temperature range from 295 K to 20 K: The Raman B mode at $31cm^{-1}$ softens as the temperature is decreased down to $T_c = 132$ K.

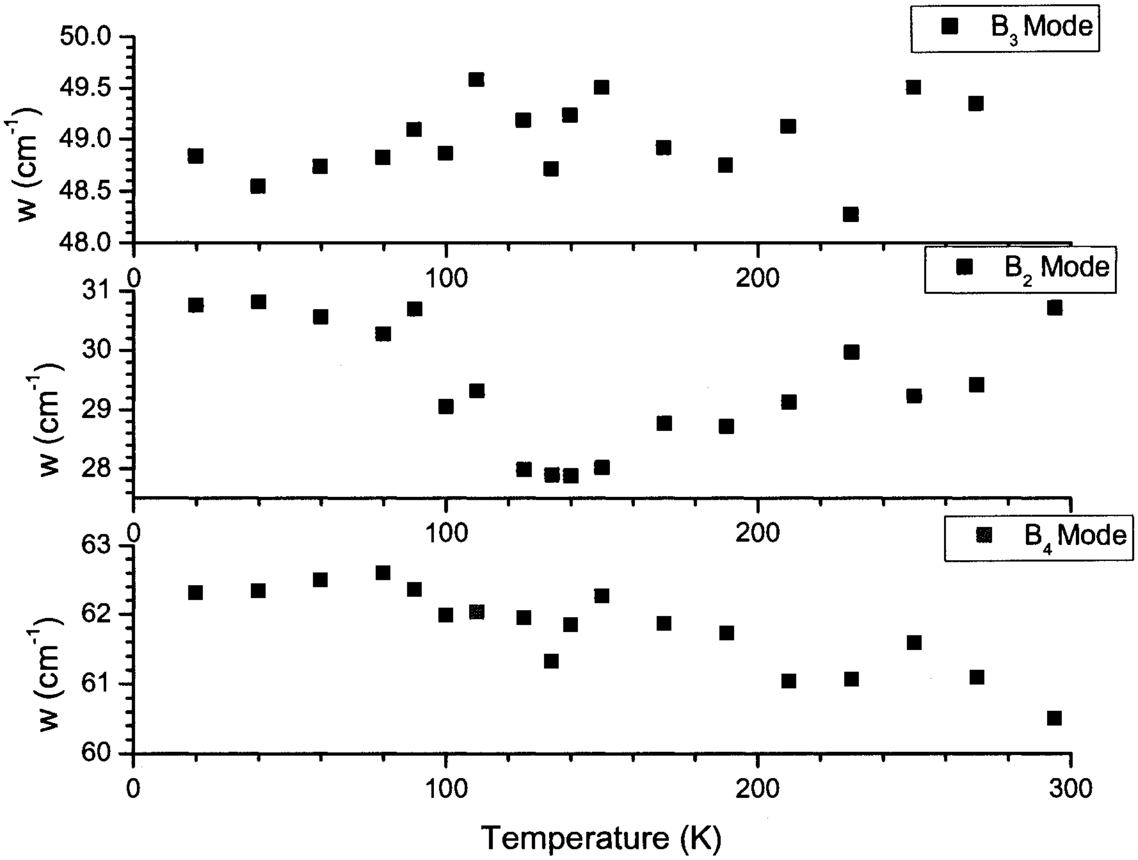

Figure 5.2: Frequencies of the B symmetry ν_2, ν_3, and ν_4 modes as a function of temperature measured using right-angle geometry. The uncertainty for the frequency of the Raman modes is 0.3 cm^{-1} while the uncertainty associated with the temperature is 0.1 K. The B symmetry ν_2 mode shows softening while the other two modes do not.

5.2 Polarized Back-scattering Raman Spectra of the B symmetry ν_2 Mode of RLHS

Polarized back-scattering Raman measurements were performed on RLHS in the temperature range from 285 K to 60 K. Back-scattering geometry was $z(sp)\bar{z}$ where the polarization of the incident light was along the [110] direction whereas the polarization of the scattered light was along the $[1\bar{1}0]$ direction. Scattered light was collected in the frequency range from 0 to 54 cm^{-1} in order to observe the Rayleigh line, and the ν_2 mode (B mode at 31 cm^{-1}). An attenuator was used to decrease the power of the incident light, and the dwell time of the photon counter was set to 1 second in the range from 0 to 18 cm^{-1}, where only the Rayleigh line was observed, and it was used to calibrate the frequency of the B symmetry ν_2 mode. The dwell time for the range from 18 to 54 cm^{-1} was set to 150 s. The Raman spectrum at 230 K is shown in Fig. 5.3 as an example which includes both the Rayleigh line, and the B symmetry ν_2 mode. The Rayleigh line was fitted using a Gaussian function, then obtained values of the frequency and the line width were used in the fit of the ν_2 mode with a Lorentzian function.

Although the temperature was desired to decrease down to 20 K during the measurements, possible contraction in the cryostat due to low temperature caused a serious loss of intensity. However, 60 K, which is the lowest temperature reached during the measurements is far enough from the transition temperature $T_c = 132$ K in order to observe the temperature dependence of the optical ν_2 mode of B symmetry. Back-scattering spectra at different temperatures are displayed in Fig. 5.4, and frequencies of the ν_2 mode at these temperatures are shown in Table 5.3. The frequency of the ν_2 mode decreases from 30.6 cm^{-1} at 285 K to 28.3 cm^{-1} at T = 134 K, then, it increases up to 30.3 cm^{-1} at 60 K.

The plot of ω^2 vs. T for the B symmetry ν_2 mode is shown in Fig. 5.5 together with our results obtained from right-angle measurements, as well as those published by Mróz

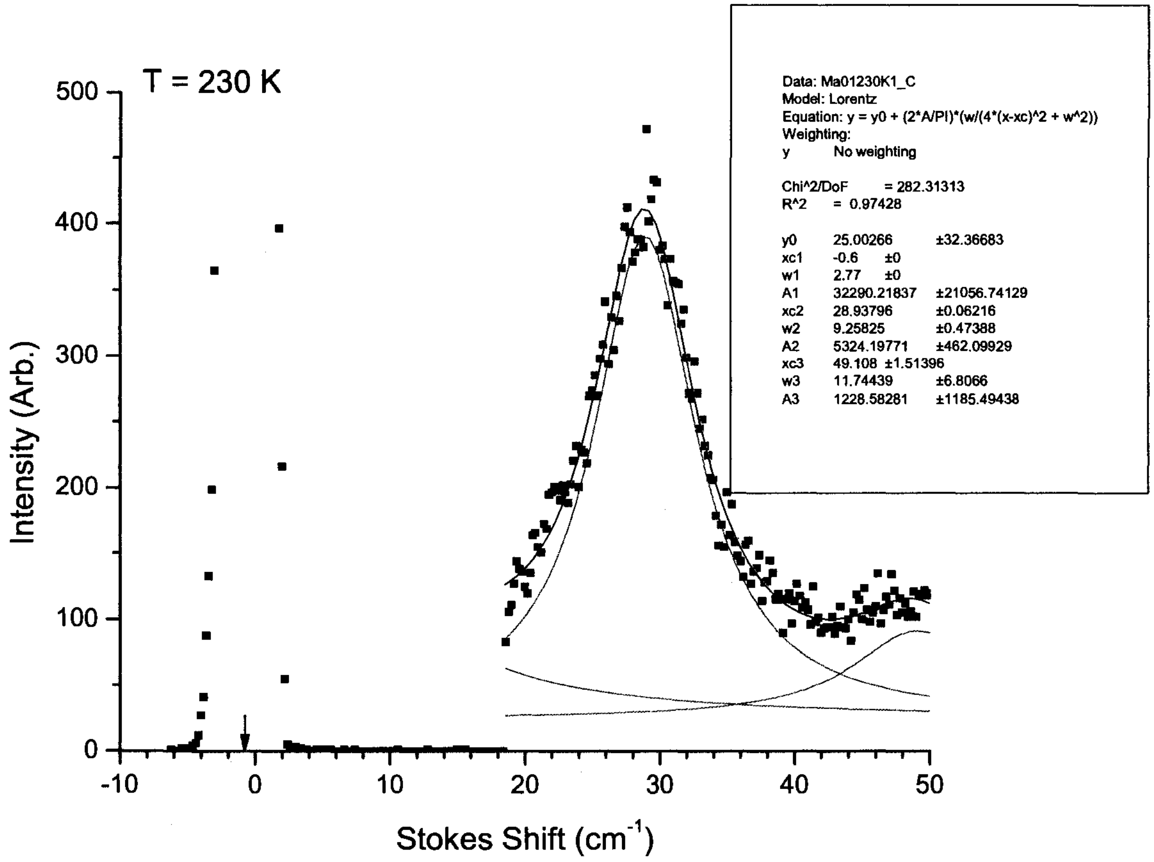

```
Data: Ma01230K1_C
Model: Lorentz
Equation: y = y0 + (2*A/PI)*(w/(4*(x-xc)^2 + w^2))
Weighting:
y        No weighting

Chi^2/DoF      = 282.31313
R^2     =  0.97428

y0       25.00266         ±32.36683
xc1      -0.6      ±0
w1       2.77      ±0
A1       32290.21837      ±21056.74129
xc2      28.93796         ±0.06216
w2       9.25825          ±0.47388
A2       5324.19771       ±462.09929
xc3      49.108  ±1.51396
w3       11.74439         ±6.8066
A3       1228.58281       ±1185.49438
```

Figure 5.3: Polarized Raman Spectrum at 230 K with back scattering geometry. The position and the width of the Rayleigh line (shown with the red arrow) was determined by a fit to a Gaussian profile and was used to calibrate the frequency of the B symmetry ν_2 mode. The peak position of the Raman mode was determined by a fit of the data to the Lorentzian function, $y = y_o + \frac{2A}{\pi}\frac{\omega}{4(x-x_c)^2+\omega^2}$ where y_o is the baseline offset, A is the total area under the curve from the baseline, x_c is the center of the peak, and ω is the full width of the peak at half height. The parameters x_{c1} and ω_1 correspond to the peak position and width of the Rayleigh line while x_{c2}, ω_2, ω_3, and x_{c3} are those associated with the B symmetry ν_2 and ν_3 modes.

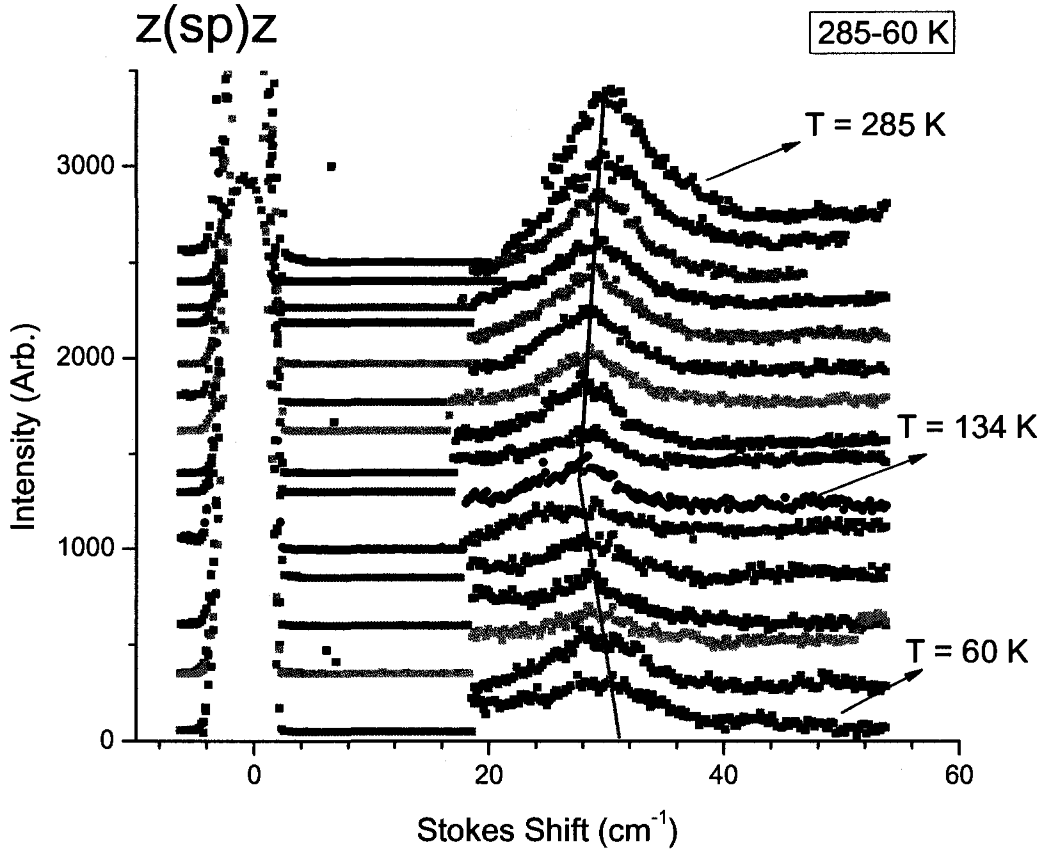

Figure 5.4: Back-Scattering Raman Spectra of the B symmetry ν_2 mode in the temperature range from 295 K to 20 K: The scattering geometry is $z(sp)\bar{z}$. The Raman B symmetry ν_2 mode softens as the temperature is decreased down to T_c = 132 K, and its frequency increases as the temperature is decreased below T_c.

et. al. [26]. For the back scattering case, the slopes of the linear fit for ω^2 vs. T are $s_{high} = 0.9 \pm 0.1$, and $s_{low} = 1.9 \pm 0.3$ above and below T_c, respectively. These values are consistent with results obtained from the right-angle scattering measurements. The slopes obtained above T_c for both of the present results is also consistent with data from Mróz et. al. [26]. The standard deviation for the fit to the right-angle results was twice as large as that from the back scattering measurements. Hence, the back scattering experiments provided a more precise measure of the temperature dependence of the B symmetry ν_2 mode frequency.

As seen in Fig. 5.5, the frequency of the B symmetry ν_2 mode does not go to zero at T_c. In Chapter 4, we introduced the temperature T_o, called the stability limit, at which the optical mode frequency goes to zero. The extrapolation of the high temperature fit shows that $T_o = -789$ K, which means that the B symmetry ν_2 mode never goes to zero as T_o is below the absolute temperature. However, $T_c - T_o = 921$ K gives a measure of the strength of the bilinear coupling between the order parameter and the spontaneous strain. This value is compared to those obtained from other pseudoproper ferroelastic compounds listed in section 5.3.

5.3 Discussion

Our Raman scattering measurements, with both right-angle and back-scattering geometries, reveal that the Raman active B symmetry ν_2 mode shows softening. However, data obtained from back scattering measurements had less uncertainty than that of the right angle results. The square of the frequency of that mode decreases linearly as a function of temperature above T_c while it increases below T_c. The ratio of the slopes for ω^2 vs. T was found to be -2:1, indicating that the transition in RLHS is pseudoproper ferroelastic. In Chapter 4, a Landau model for a pseudoproper ferroelastic phase transition was presented. According to this model, the order parameter is associated with a *B* symmetry soft optic mode which

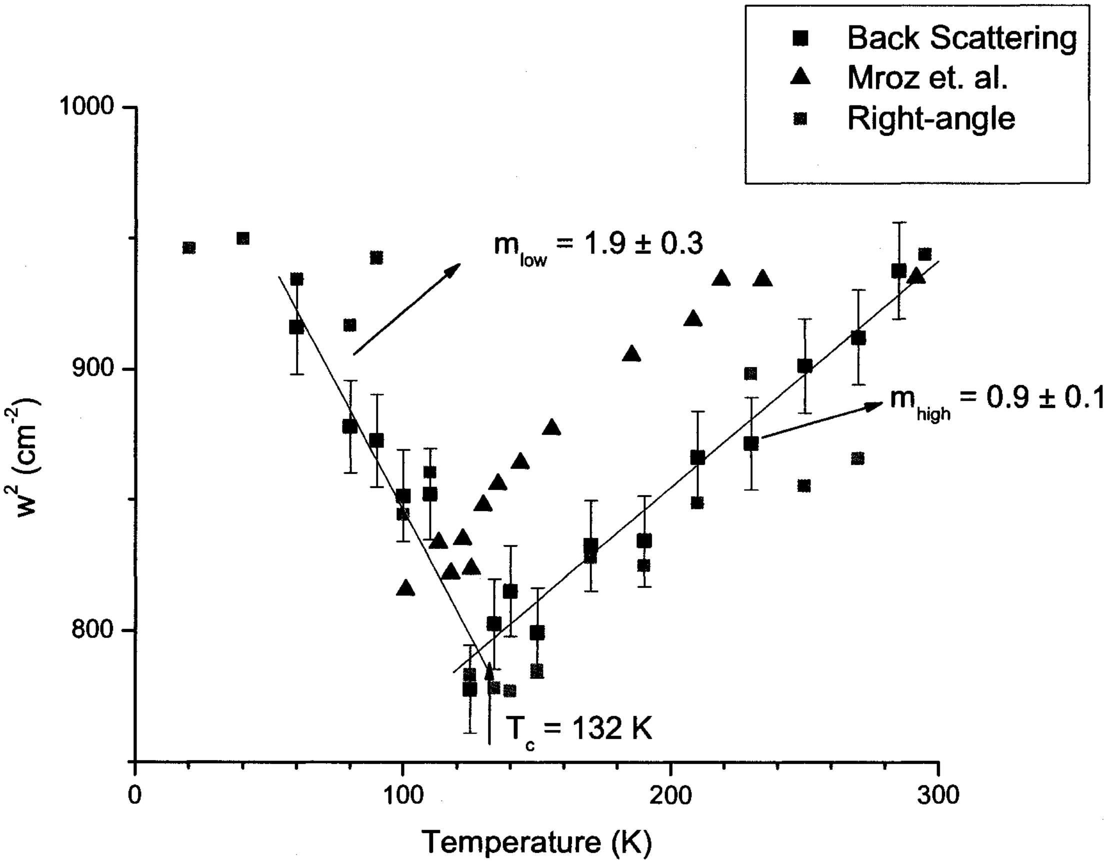

Figure 5.5: ω^2 as a function of temperature: The black points correspond to the back scattering data, the red points are from the right-angle scattering measurements, and the blue points are from Mróz et. al. [26].

belongs to the space group $P4_1$. The model also predicts that the ratio of the slopes of the squared optic mode frequency vs temperature below and above T_c is -2:1. Considering that the Landau model for the $4 \rightharpoonup 2$ ferroelastic phase transition [19] also accounts for the elastic properties of RLHS, our observation for the temperature dependence of the optical B symmetry ν_2 mode confirms the validity of the ferroelastic model by Quirion et. al. [19]. As a result, the ferroelastic phase transition in RLHS at $T_c = 132$ K is pseudoproper ferroelastic.

According to the pseudoproper ferroelastic model, the order parameter couples bi-linearly with the spontaneous strain e_s. This results in the incomplete softening of the optical B symmetry ν_2 mode (at 31 cm^{-1}) associated with the order parameter as observed by our experiments. The frequency of the optic mode goes to zero at $T_o = -789$ K, called the stability limit [2], in the absence of coupling with the strains. The stability limit T_o was calculated by extrapolating the high temperature linear fit down to ω equal zero. According to our analysis, $T_c - T_o = 921$ K. The strength of the coupling has also been calculated for other pseudoproper ferroelastic compounds where $T_c - T_o = 228$ K for $BiVO_4$ [22], $T_c - T_o = 260$ K for LaP_5O_{14} [2], and $T_c - T_o = 137$ K for $KH_3(SeO_3)_2$ [21]. This shows that the magnitude of the strength of the coupling in RLHS is significantly larger than the value determined for other pseudoproper ferroelastic compounds. Considering that T_o is calculated as $T_o = -789$ K, the complete softening of the soft B mode can never be observed. If T_o was above the absolute temperature, external uniaxial stress which accounts for spontaneous strain could be applied to maintain a single domain phase. According to Wolejko et. al. [5], that uniaxial stress for RLHS is along the [100] or [010] directions. However, as T_o is below the absolute temperature, complete softening of the optical B (ν_2) mode can never be observed.

Table 5.2: Frequencies (in cm^{-1}) of the optical B symmetry ν_2, ν_3, and ν_4 modes in RLHS measured using right angle geometry in the temperature range from 295 to 20 K.

Temperature (K)	ν_2 Mode	ν_3 Mode	ν_4 Mode
295	30.7	47.7	60.5
270	29.4	49.4	61.1
250	29.2	49.5	61.6
230	30	48.3	61.1
210	29.1	49.1	61.0
190	28.7	48.8	61.7
170	28.8	48.9	61.9
150	28.0	49.5	62.3
140	27.9	49.2	61.9
134	27.9	48.7	61.3
125	28.0	49.2	62.0
110	29.3	49.6	62.0
100	29.1	48.9	62.0
90	30.7	49.1	62.4
80	30.3	48.8	62.6
60	30.6	48.7	62.5
40	30.8	48.6	62.4
20	30.8	48.8	62.3

Table 5.3: Frequencies (in cm^{-1}) of the optical ν_2 mode of B symmetry in RLHS measured using back scattering geometry in the temperature range from 285 to 60 K.

Temperature (K)	ν_2 mode
285	30.6
270	30.2
250	30
230	29.5
210	29.4
190	28.9
170	28.9
150	28.3
140	28.6
134	28.3
125	27.9
110	29.2
100	29.2
90	29.5
80	29.6
60	30.3

Chapter 6

CONCLUSION

In this project, Raman scattering measurements were performed on the ferroelastic compound $Rb_4LiH_3(SO_4)_4$ in order to reveal the nature of the ferroelastic phase transition at 132 K. Frequency of the optical B symmetry modes was measured as a function of temperature using an Ar-Ion laser, a double grating spectrometer and a cryogenic system. Both right-angle and back scattering geometries were employed during the measurements. The temperature range in our investigation was 20-295 K for the right-angle geometry while it was 60-285 K for back scattering experiments.

Although its elastic properties has been studied in detail, the driving mechanism for the ferroelastic phase transition in RLHS at about $T_c = 132$ K is still controversial. Various groups proposed two classes of Landau models associated with the $4 \rightharpoonup 2$ ferroelastic phase transition in order to identify the nature of the transition. One assumes that the driving mechanism for the transition is the spontaneous strain as described by a proper ferroelastic Landau free energy [13, 18, 19]. Other class assumes that the order parameter is another physical quantity with the same symmetry as the spontaneous strains [11, 19]. In this case, the transition is pseudoproper ferroelastic. The pseudoproper ferroelastic model by Quirion et. al. [19], which quantitatively agrees with experimental results, indicates that the phase transition is driven by softening of an optical B mode. As a result, we performed Raman scattering measurements to identify the true nature of the phase transition in RLHS.

Our Raman scattering measurements with both right-angle and back-scattering geometries show that the Raman active B mode at $31cm^{-1}$ (ν_2 mode of B symmetry) softens although the back scattering geometry provided with spectra much less background. The square of the frequency of B mode shows linear temperature dependence below and above T_c. The ratio of the slopes of the linear fits for the frequency square of the B mode against the temperature, ω^2 $vs.$ T, was found to be -2:1, which is in agreement with the pseudoproper ferroelastic model proposed by Quirion et. al. [19]. The optical B mode did not show complete softening due to the bilinear coupling of the B mode with the spontaneous strain e_s. The temperature at which the soft B mode goes to zero was calculated by the extrapolation of the linear fit for ω^2 T above T_c, and it was obtained that $T_c - T_o = 925$. The strength of the coupling was also calculated for other pseudoproper ferroelastic compounds where $T_c - T_o = 228$ K for $BiVO_4$ [22], $T_c - T_o = 260$ K for LaP_5O_{14} [2], and $T_c - T_o = 137$ K for $KH_3(SeO_3)_2$ [21]. This shows that the magnitude of strength of the coupling is significantly larger than other pseudoproper ferroelastic compounds. As T_o is below zero kelvin, complete softening of the B mode cannot be observed even when uniaxial stress is applied to obtain a single domain phase in RLHS below T_c.

By our Raman measurements measurements, it was concluded that the phase transition in RLHS at $T_c = 132$ K is pseudoproper ferroelastic. The ferroelastic compound $(NH_4)_4LiH_3(SO_4)_4$ which shows similar elastic properties was previously analyzed within the framework of a proper ferroelastic model. We believe that Raman measurements are necessary in order identify the nature of the ferroelastic phase transition in $(NH_4)_4LiH_3(SO_4)_4$ at $T_c = 232$ K.

Appendix A

High Frequency (Internal) Raman Modes observed by Back Scattering

Polarized Raman spectra of RLHS were also measured in the frequency range from 200 to 1400 cm^{-1} with back scattering geometry $z(sp)\overline{z}$ at 4 different temperatures above and below the phase transition temperature. These data are presented here as complimentary information with the expectation that they may be of value for future extension of the work.

The spectra were taken with 1 cm^{-1} step size at 290, 134, 100, and 20 K. The four spectra are displayed in Fig. A.1. The frequency ranges from 350 to 550 cm^{-1} and 850 to 1150 cm^{-1} were further investigated with 0.2 cm^{-1} step size at 290, 134, and 20 K. These spectra are shown in Fig. A.2 and A.3. Results are compared with those from Baran et. al. [24] and are shown in Table A.1. The first column gives the modes by Baran et. al. [24] with the scattering geometry employed. The second, third, fourth, and fifth columns give the frequency of the modes measured at 290 K, 134 K, 100 K, and 20 K. Modes observed by Baran et. al. [24] using the $y(xx)z$ scattering geometry may be of A or B symmetry species. Modes observed with the $y(xy)z$ geometry belong to the B symmetry. As the scattering geometry in our experiments was $z(sp)\overline{z}$, where the polarization of the incident and the scattered light were along [110] and $\bar{1}10$, the observed modes may be of A or B symmetry species. As a result, the symmetry of the modes presented in Table A1 depends on the geometry used. to observe these modes. The mode at 523 cm^{-1} is an A mode as it was observed by Baran et al. [24] using the y(zz)x geometry. Moreover, modes at 489 cm^{-1} and 1102 cm^{-1} were not observed by Baran et. al. [24]. Although the modes observed in the HS phase are A or B symmetry species, all of the modes become those of A symmetry species in the LS phase. According to Baran et. al. [24], all modes are stretching vibrations of SO_4^{-2} ions except for two modes at 1046, and 890 cm^{-1}. The mode at 1046 cm^{-1} is due to the stretching vibration of SO_4^{-2} ions and SO_3 which has a short hydrogen bond. The mode at 890 cm^{-1} also results from SO_4^{-2} ions together with $S - O_H$. As the temperature was lowered from T = 290 K, some of the modes showed splitting just above T_c. These modes at 439, 636, and 982 cm^{-1} split into two separate modes which belong to A symmetry species below T_c. Some of the modes, namely, those at 455, 489, 890, 1046, and 1166 cm^{-1} split below T_c. Splitting of the modes at 455, 489, 890, 1046 were observed at 20 K. The reason for not observing the splitting of these modes at 100 K might be the large step size of the experiments.

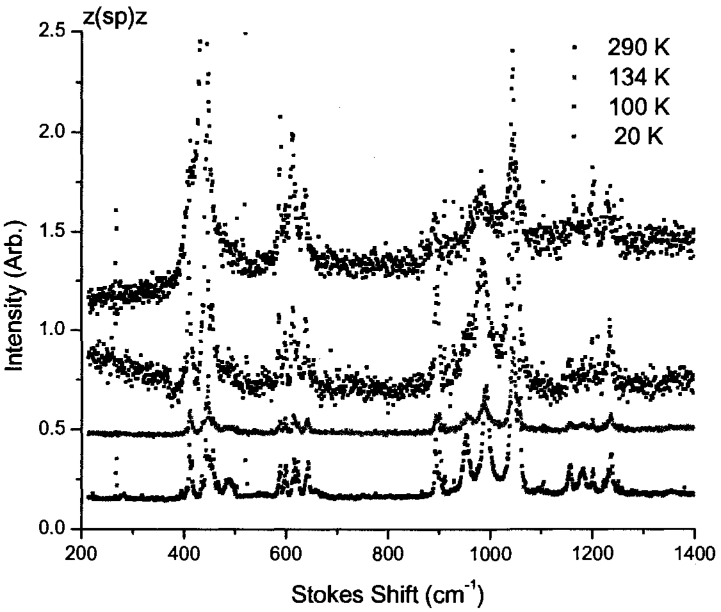

Figure A.1: Spectra in the 200-1400 cm^{-1} range observed by back scattering geometry above and below T_c. Spectra were measured at 290, 134, 100, and 20 K.

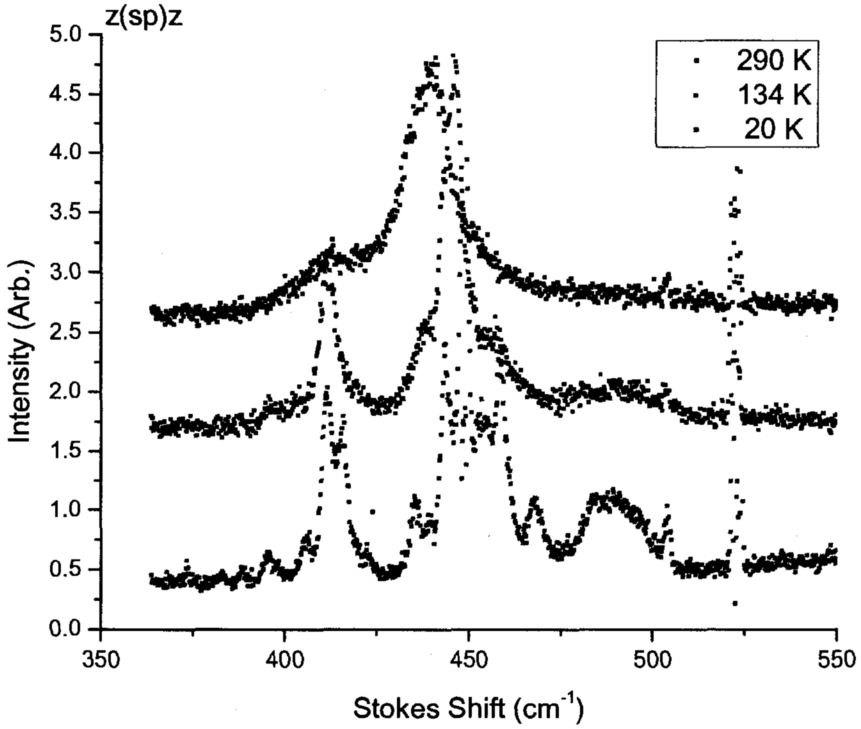

Figure A.2: Spectra in the 350-550 cm^{-1} range observed by back scattering geometry at 290, 134, and 20 K.

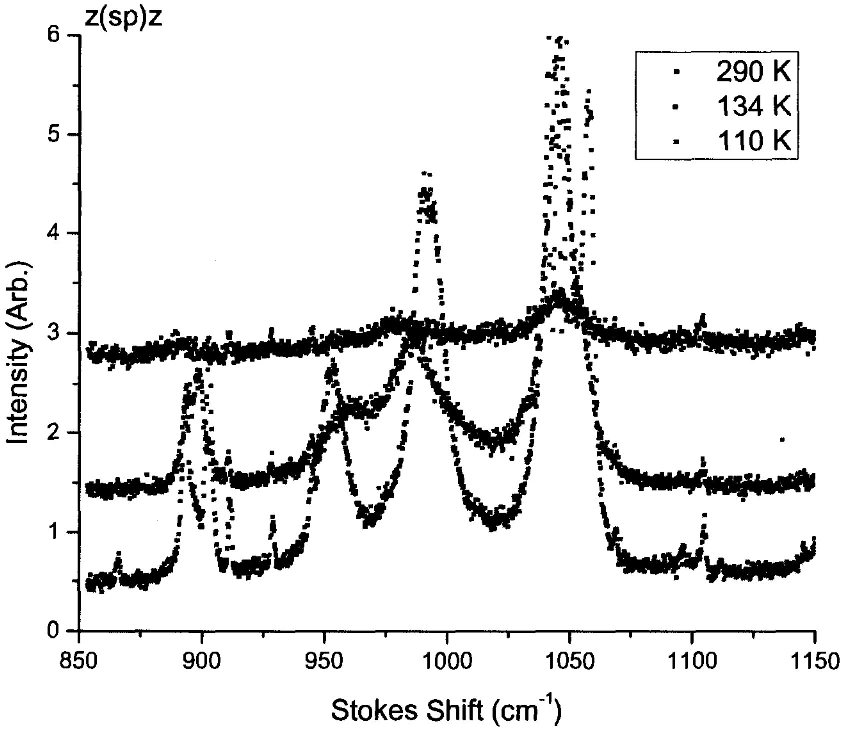

Figure A.3: Spectra in the 850-1150 cm^{-1} range observed by back scattering geometry at 290, 134, and 20 K.

Table A.1: Frequencies (in cm^{-1}) of the internal modes observed at 200-1400 cm^{-1} at 290, 134, 100, and 20 K and the results from Baran et. al. [24] at 300 K. In the column including the data from Baran et. al. [24], the scattering geometry used was also written before the frequency shift of the mode. Both A and B symmetry modes were observed during the measurements with $z(sp)\bar{z}$ geometry where s and p are the polarization of the incident and scattered light along the [110] and [$1\bar{1}0$] directions, respectively.

Baran et. al.	This Work			
T = 300 K	T= 290 K	T = 134 K	T = 100 K	T = 20 K
y(xx)z 411, y(xy)z 410	411	412	412	412
y(xx)z 441, y(xy)z 441	439	436, 446	447	435, 448
y(xy)z 449	455	458	457	458, 468
	489	490	490	489,504
y(zz)x 521	523	522	523	523
y(xx)z 588, y(xy)z 588	589	588	588	589
y(xx)z 597, y(xy)z 597	598	599	599	600
y(xy)z 612	613	615	616	617
y(xy)z 636	636	624, 641	642	625, 644
y(xx)z 888, y(xy)z 888	890	897	897	893,902
y(xx)z 982	982	987,958	989, 955	953,992
y(xx)z 1043, y(xy)z 1043	1046	1046	1046	1045,1057
	1102	1104	1106	1104
y(xx)z 1163, y(xy)z 1163	1166	1156	1158, 1182	1157, 1182
y(xx)z 1200	1201	1201	1201	1202
y(xx)z 1227, y(xy)z 1230	1232	1236	1236	1236

Bibliography

[1] K. Aizu, J. Phys. Soc. Japan **27**, 387 (1969).

[2] V.K. Wadhawan, Phase Transitions **3**, 3 (1982).

[3] E.K.H Salje, *Phase Transitions in Ferroelastic and Co-Elastic Crystals* (Cambridge University Press, Cambridge, 1993).

[4] V. K. Wadhawan, *Introduction to Ferroic Materials* (Gordon and Breach Science Publishers, Singapore, 2000).

[5] T. Wolejko, P. Pisunowicz, T. Breczewski, and T. Krajewski, Ferroelectrics **81**, 175 (1988).

[6] M. Polomska and F. Smutny, Phys. Stat. Sol. (B) **154**, K103 (1989).

[7] M. Polomska, A. Pawlowski, F. Smutny, and J. Wolak, Ferroelectrics **140**, 299 (1993).

[8] B. Mróz, S. M. Kim, B. M. Powell, H. Kiefte, and R. L. Donaberger, Phys. Rev. B **55**, 17 (1997).

[9] M. Polomska, and F. Smutny, Ferroelectrics **111** Part B, 237 (1990).

[10] M. Polomska, and A. Pawlowski Ferroelectrics **157**, 93 (1994).

[11] B. Mróz, J. A. Tuszynski, H. Kiefte, and M. J. Clouter, J. Phys.:Condens. Matter **1**, 4425 (1989).

[12] T. Wolejko, G. Pakulski, Z. Tylczynski, *Ferroelectrics **81**, 179 (1988).*

[13] B. Mróz, H. Kiefte, M. J. Clouter, J. A. Tuszyński, J. Phys.:Condens. Matter **3**, 5673 (1991).

[14] F. J. Zúniga, G. Extebarria, G. Madariaga, T. Breczewski, Acta Cryst. C **46**, 1199 (1990).

[15] P. Tolédano, M. M. Fejer, B. A. Auld, Phys. Rev. B **27**, 9 (1983).

[16] V. Janovec, V. Dvořák, J. Petzelt, Czech. J. Phys. B, **25**, 1362 (1975)

[17] J. Tolédano, P. Tolédano, Phys. Rev. B **21**, 3 (1980).

[18] P. Piskunowicz, T. Breczewski, and T. Wolejko, Phys. Sol. Sol. A **114**, 505 (1989).

[19] G. Quirion, W. Wu, J. Rideout, *Landau model for the elastic properties of the ferroelastic crystal $Rb_4LiH_3(SO_4)_4$*, arXiv.cond-mat/0606064 (unpublished) (2006).

[20] W. Wu, *Investigation of the Elastic Properties of $Rb_4LiH_3(SO_4)_4$ as a Function of Temperature and Pressure* (M.Sc. Thesis, Dept. of Physics, MUN, 2004).

[21] Y. Mikita, F. Sakurai, T. O saka, and I, Tatsuzaki, J. Phys. Sc. Jpn. **42**, 518 (1977).

[22] A. Pinczuk, G. Burns, and F. H. Dacol, Solid State Commun. **24**, 163 (1977).

[23] William I F David, J. Phys. C:Solid State Phys. **16**, 5093 (1983).

[24] J. Baran, M K. Marchewska, H. Ratajczak, Z. Czapla, Journal of Molecular Structure **436-437**, 281 (1997).

[25] M. K. Marchewka, J. Baran, Spectrochimica Acta Part A **60**, 201 (2004).

[26] B. Mróz M. Kaczmarski, H. Kiefte, and M. J. Clouter, J. Phys: Condens. Matter **4**, 7515 (1992).

[27] A. Andersen, *The Raman Effect, Volume 1: Principles* (Marcel Deccer Inc., Newyork, 1971).

[28] J. R. Ferraro, K. Nakamoto, C. W. Brown, *Introductory Raman Spectroscopy,* 2^{th} *Edition* (Academic Press, 2003).

[29] E. Gregoryanz, *Raman and Brillouin Spectroscopic Studies of Single Crystals of* CH_4 *and* CD_4 (Ph.D. Thesis, Dept. of Physics, MUN, 1998).

[30] Facilities at the University of Bath, Introduction to Raman Spectroscopy, available at http://people.bath.ac.uk/pysdw/newpage11.htm (July 4th, 2008) .

[31] R. Loudon, Adv. in Phys. **13**, 423 (1964).

[32] J. C. Decius, and R. M. Hexter, *Molecular Vibrations in Crystals* (McGraw-Hill Inc., 1977).

[33] T. C. Damen, S. P. S. Porto, and B. Tell, Phys. Rev. **142**, 2 (1966).

[34] J. F. Nye, *Physical Properties of Crystals: their representation by tensors and matrices* (Clarendon Press, 1984).

[35] Paul Scherrer Institute, Laue Orient Express website, http://laue.web.psi.ch/laue-determination.htm (June 15th, 2008)

[36] D. W. Feldman, James H. Parker, Jr., W. J. Choyke, Lyle Patrick, Phys. Rev. **170**, 3 (1968).

[37] G. Morandi, F. Napoli, E. Ercolessi, *Statistical Mecahanics* (World Scientific, 2001).

[38] M. Bromberek, *Elastic Properties of Ferroelastic LiKSO4 in the Temperature Range from 20 K to 150 K* (M.Sc Thesis, Dept. of Physics, MUN, 2001).

[39] L.D. Landau, E.M. Lifshitz, *Statistical Physics* (Pergamon Press, 1969).

[40] M. Tinkhan, *Group Theory and Quantum Mechanics* (Dover Publications, New York, 2003).

[41] N. N. Ovsyuk, S. V. Goryainov, Europhys. Lett. **64** (3), 351 (2003).

[42] S. A. T. Redfern, E. Salje, J. Phys. C:Solid State Phys **21**, 288 (1988).

[43] A. Sawada, M. Udagawa, T. Nakamura, *Phys. Rev. Letters* ***39**, 13 (1977).*

[44] H. Hellwig, A.F. Goncharov, E.Gregoryanz, H. K. Mao, and R. J. Hemley, Phys. Rev B **67**, 174110 (2003).

[45] G. Errandonea and H. Savary, *Phys. Rev B* ***24**, 1292 (1981).*

[46] E. Dieulasaint, and D. Royer, *Elastic Waves in Solids* (John Wiley and Sons Ltd., 1980).